Compact Two-color Ultrafast Yb:fiber Chirped Pulse Amplifiers and Mid-infrared Generation Based on Difference Frequency Generation

by

Tuyen Hoang

A thesis

presented to the University of Waterloo

in fulfillment of the

thesis requirement for the degree of

Master of Science

in

Physics

Waterloo, Ontario, Canada, 2018

© Tuyen Hoang 2018

This thesis consists of material all of which I authored or co-authored: see Statement of Contributions included in the thesis. This is a true copy of the thesis, including any required final revisions, as accepted by my examiners.

I understand that my thesis may be made electronically available to the public.

Statement of Contributions

A part of my thesis which is setting up the experiment of the chirped pulse amplification and mid-infrared generation was contributed by a co-worker, Xinyang Su.

Abstract

A powerful mid-infrared frequency comb in the 2-20 μm range plays a very important role in the development of optical frequency metrology, spectroscopy and other fields of technology. However, there is a big gap in the long wavelength range from 10 to 40 μm mainly because of technical challenges. Difference frequency generation has been shown to be able to generate a frequency comb due to its ability to cancel the carrier-envelope phase shift from pulse to pulse. In this thesis, the first task is to develop a compact and powerful two-color chirped pulse amplification system consisting of two Yb:fiber amplification stages. Such system is compact, stable and highly efficient by utilizing a chirped fiber Bragg grating, a all-normal dispersion photonic crystal fiber and fiber splicing. The chirped fiber Bragg grating generates a two-color signal from the supercontinuum produced in the photonic crystal fiber. An average power of 3.5 W of the two-color signal composed of two peaks at 1025 and 1085 nm is achieved after the main Yb:fiber amplifier stage. Moreover, the power ratio between the 1025 and 1085 nm wavelengths can be tunable. Particularly, the best short:long power ratio obtained is 2:1. The second task is to generate a mid-infrared wavelength of around 18 μm in a 1 mm GaSe crystal by employing the difference frequency generation technique. The generated mid-infrared power is in the range of 150-180 μW. Finally, the optical cross correlation technique to measure the timing jitter of the femtosecond Yb:fiber laser at a 65MHz repetition rate is applied for the purpose of synthesizing a frequency comb at the wavelength of 18 μm. We conclude that this Yb:fiber laser could not make a frequency comb due to its high timing jitter at around 450 fs.

Acknowledgements

First of all, I would like to thank my supervisor, Professor Donna Strickland, for giving me an opportunity to join her research group, for her guidance, help and support during my MS.c study.

I would like to thank the members of the supervisory committee, Professors Melanie Campbell, David Yevick, Joe Sanderson, Safieddin Safavi-Naeini, and my research group members for all the assistance and helpful feedback provided throughout my MS.c at University of Waterloo.

Last but not least, a very special thank to Professor John Berlinsky, my parents, my sister and my children for their great support and encouragement.

Contents

List of Figures

Nomenclature

MIR	Mid-infrared
IR	Infrared
DFG	Difference frequency generation
OPO	Optical parametric oscillation
QCL	Quantum cascade laser
CPA	Chirped pulse amplification
PCF	Photonic crystal fiber
CFBG	Chirped fiber Bragg grating
GDD	Group delay dispersion
CEP	Carrier-envelope phase
ASE	Amplified Spontaneous Emission
SOD	Second-order dispersion
TOD	Third-order dispersion
MCT	HgCdTe (Mercury Cadmium Telluride)
SC	Supercontinuum
GVD	Group velocity dispersion
PBS	Polarizing beam splitter
FWHM	Full width at half maximum
BBO	β-barium borate
SHG	Second harmonic generation
Ge	Germanium
GaSe	Gallium selenide
AND	All-normal dispersion
FBG	Fiber Bragg grating

HWP	Half wave plate
SPM	Self phase modulation
TPA	Two photon absorption

1 Introduction

1.1 Motivation

The inspiration for this thesis came from utilizing optical femtosecond frequency combs in applications such as frequency metrology and spectroscopy. Steven T. Cundiff and Jun Ye pointed out in [1] that optical frequency combs have *"revolutionized optical frequency metrology and synthesis"* (Cundiff 1).

Optical frequency metrology is the science of accurately measuring frequency [2]. For the purpose of accuracy, absolute frequencies should be measured directly rather than indirectly via their corresponding wavelengths. Traditionally, absolute frequencies are measured via harmonic frequency chains. This method requires an atomic clock to set the lower end of the chain [3]. This low-end frequency is very stable and produced by a frequency standard which is included in the clock [4]. Then, higher harmonics of that frequency are produced in nonlinear crystals or other instruments [3]. However, frequencies set by atomic clocks are limited in the range of a few GHz or in other words they are available only in the microwave range [4]. This limitation is solved by using optical clocks which can offer a working frequency range of several hundreds of THz. However, signals generated in ranges of hundreds of THz by optical clocks oscillate too fast compared to signals generated by available electronic devices [4]. Besides, employing frequency chains, either in atomic or optical clocks, requires setting up complicated and labor intensive apparatuses. Moreover, utilizing harmonic frequency chains allows only one optical frequency to be measured at a time [3, 4]. These all problems that optical frequency metrology encountered have been resolved after 30 years since the first chain was produced thanks to the 'birth' of optical frequency combs. They not only help simplify the system, with only one single device - that is mode-locked lasers, while still cover a significant wider spectrum range, hundreds of THz, but also give reliable measurements [4].

A Frequency comb is a spectrum that is composed of sharp and equally spaced spikes in the frequency domain of a mode-locked laser. The space between any two adjacent comb lines is determined by the repetition rate f_{rep} or inverse of the round trip time of the pulses in the cavity, $\frac{1}{T_{RT}}$. However, in reality, it is not true that all of the mode-locked lasers can generate a frequency comb. In order to have a full explanation of this issue, it is useful to discuss about electromagnetic fields generated by a mode-locked laser in the time domain and frequency domain. As is illustrated by Figure 1.1, in the time domain, the output of a mode-locked laser, theoretically, is a train of identical pulses. The temporal space between any arbitrary adjacent pulses in the train is equal to the amount of time that it takes a pulse to complete a round trip in the cavity at a group velocity of v_g. This amount of time is called period $T_{RT} = \frac{v_g}{2L}$. The period, and therefore the repetition rate, do depend on the group velocity and the cavity length L [3]. Accordingly, Fourier series expansion of the pulse train leads to a frequency comb in the frequency domain where the space between the comb lines equals f_{rep} [5]. In addition, underneath each envelope of a pulse, the electric field $E(t)$ of the carrier or central frequency oscillates at a frequency of ω_0. The offset between the peak of the envelope and that of the carrier is called carrier-envelope phase

$\phi_{CE} = \Delta t \cdot \omega_0$ (shown in Figure 1.2), often abbreviated as CEP. So, $E(t)$ can be written in the time domain as

$$E(t) = A(t)\cos(\omega_0 t + \phi_{CE}) \tag{1}$$

where $A(t)$ is the envelope function. It is maximized when t=0 [6]. In fact, unfortunately, pulses in the train are not identical because ϕ_{CE} is not a constant from pulse to pulse. The slipping in the CEP causes a phase change between the pulses, $\Delta\phi_{CE}$. The reason for this phase shift lies in the fact that pulses travel in a dispersive medium where its refractive index depends on the light's wavelength. In such medium of length L, the carrier propagates at phase velocity of v_{ph} which is different from v_g, and so the phase is a function of frequency, i.e.

$$\phi(\omega) = -\frac{n(\omega)\,\omega L}{c} \tag{2}$$

where c is the speed of light. By taking derivative of equation (2) with respect to ω, we get [6]

$$\frac{1}{v_g} = \frac{1}{v_{ph}} + \frac{dn(\omega)}{d\omega}\frac{\omega}{c} \tag{3}$$

In fact, the CEP shift is dominated by the second term in equation (3) rather than the negligible difference between phase velocity and group velocity [6]

$$\Delta\phi_{CE} = \left[L\frac{\omega^2}{c}\frac{dn(\omega)}{d\omega}\right] \mod 2\pi \tag{4}$$

Correspondingly, in the frequency domain, the non-zero offset $\Delta\phi_{CE}$ leads to a non-zero offset frequency (Figure 1.3). Hence, the whole frequency comb is shifted by an amount of [6]

$$f_0 = \frac{\Delta\phi_{CE}}{2\pi} f_{rep} \tag{5}$$

In consequence, a frequency comb cannot be formed if either T_{RT} or $\Delta\phi_{CE}$ is not a constant.

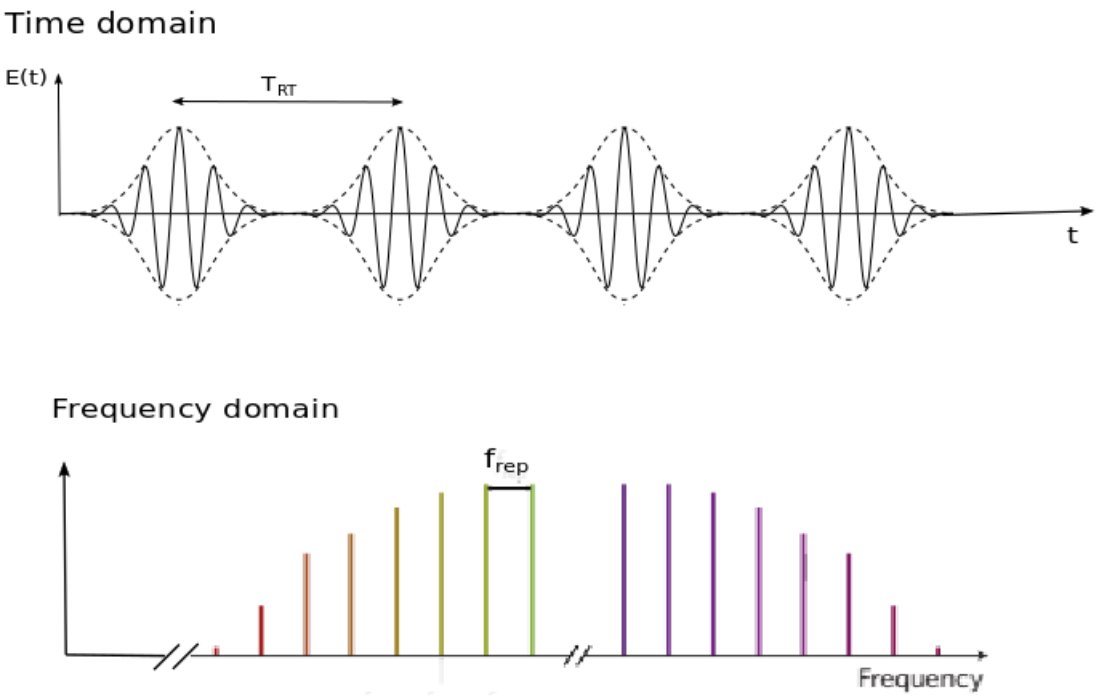

Figure 1.1: Electromagnetic fields generated by a mode-locked laser in the time and corresponding frequency domain

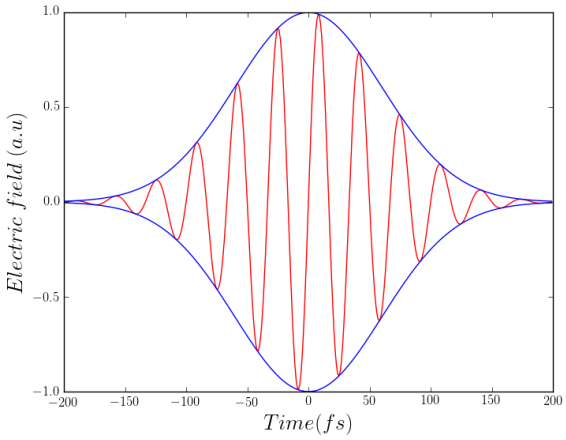

Figure 1.2: A pulse with $\phi_{CE}=\frac{\pi}{2}$

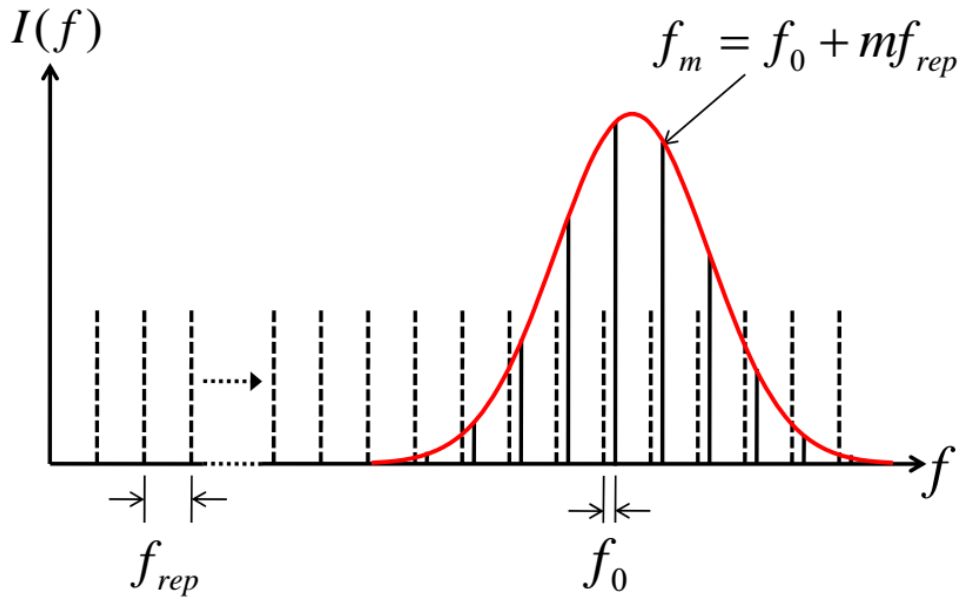

Figure 1.3: The shifted frequency comb

If a mode-locked laser is qualified for making a frequency comb, its frequency comb can be used as an optical "ruler" to measure unknown frequencies. Such "ruler" is required not only to be highly stable but also to have a broad bandwidth [7]. Fortunately, frequency comb synthesizers in the microwave region have been made commercially available [5] and those in the visible and near-infrared domains have been employed in frequency metrology [7]. However, the gap of commercial frequency comb generators in the mid-infrared (MIR) region, specifically in the fingerprint 2-20 μm, and especially the absence of frequency combs in the region 18-20 μm, have negatively affected or even prevented the development of many other related potential applications. MIR spectroscopy is a typical popular example [7, 8]. A spectroscopy in this region is of high interest because it gives a better and deeper comprehension of structures of molecules because they have unique fingerprints and have strong bands of absorption in the 2-20 μm range [7, 9]. Even though the spectroscopy based on MIR frequency combs provides not only precise measurement but also high sensitivity and fast detecting [8], its performance is limited by MIR comb generators' availability.

It is because no single laser source can generate such a wide range of comb bandwidth and in reality, many mode-locked lasers fail to meet simultaneously the two keystone requirements: constant repetition rate and CEP. As a results, so far many different methods have been employed to make a desired output MIR comb either directly or indirectly from a commercial or home-built laser. The most popular methods used are femtosecond laser, difference frequency generation (DFG), Optical parametric oscillation (OPO), quantum cascade laser (QCL) and Kerr comb based on micro-resonators [7, 10].

Frequency combs were traditionally generated by femtosecond mode-locked lasers. Mode-locked lasers have become popular optical devices in synthesizing frequency combs with high output powers. However, their comb is not tunable and cannot cover a wide spectral region. In addition, the longest generated wavelength is just up to around 2.5 μm as shown in Fig 3a of [7]. In contrast to mode-locked lasers, a common feature of OPO, DFG and QCL is that they all can generate frequency combs at different wavelength regions. One advantage of OPO is that it can generate very high frequency comb power, Watt level. DFG in comparison with OPO requires a more compact system because it is mandatory for the OPO cavity to be phase locked to the oscillator [11]. In addition, DFG offers an offset free CEP naturally as long as the repetition rate is stable [12]. Although in terms of output power, combs generated by DFG have lower power than those generated by OPO, it has been shown that DFG is the only method that helps generate a frequency comb in the long range of the fingerprint, particularly 18-20 μm [7]. Furthermore, frequency combs can be made by using QCL but according to authors of [10, 13] a single QCL can not produce a wide tunable spectral range like DFG and its generated wavelengths are longer than $4\mu m$. Finally, optical micro-resonators has an advantage from its resonator length which is very small, hundreds of μm. Its output frequency combs can have a wide spectral range but still up to around 2.5 μm like mode-locked lasers [7, 10]. Besides, technical challenges are also drawbacks of this approach [10].

Consequently, my research was motivated by the necessity of filling up the gap of combs in the range of 10-40 μm plus the default ability of making a frequency comb of DFG. Accordingly, the goal of my research is, first, to generate MIR at 18.5 μm in Gallium Selenide (GaSe) crystal by mixing two different frequencies, 1025 and 1085 nm, synthesized via a chirped pulse amplification (CPA) system, second, to measure timing jitter of the Yb:laser source by intensity non-collinear cross correlation. If the Yb:laser's repetition rate is already stable then it is possible for the MIR generated at 18.5 μm via DFG to be proved to be a frequency comb. Therefore, this goal can be considered as a first step in the process of making a frequency comb at 18.5 μm.

1.2 Literature Review

In this section, we will have a brief review on MIR generation via only one method, DFG, from different laser sources, Ti:sapphire, Er:fiber and Yb:fiber lasers.

Overall, in spite of the fact that DFG can produce MIR at various wavelengths or different wide tunable spectral ranges, none of the generated MIR can cover the whole range of the fingerprint region. In the lower range of this region, there are more options in terms of non-linear crystal availability used for DFG. However, in the long range 18-

20 μm, due to the transmission limitation and efficiency of the crystals, the number of available crystals is narrowed down. GaSe crystals have been used popularly [14, 15, 16]. In addition, all of the three laser sources, Ti:Sapphire, Er:fiber and Yb:fiber lasers, can generate MIR at different wavelengths in the fingerprint region. Therefore, it is difficult to conclude which one can give more output power because the output power requires a good combination of many factors such as input power, input pulse-width and conversion efficiency of non-linear crystals, etc.

MIR wavelengths achieved via DFG from femtosecond Ti:Sapphire lasers is a tunable range from 7.5-12.5 μm. The pump and signal come from two Ti:Sapphire lasers which are synchronized to reduce timing jitter of two pulse trains down to approximately 1%. In terms of output power, [17] achieved the highest power in this spectral range for Ti:sapphire lasers, around 15 μW. The nonlinear crystal used for down frequency conversion is GaSe [17]. Under the same approach, DFG, but different laser source, mode-locked Er:fiber laser, C.Erny *et al.* obtained a range of 3.2-4.8 μm. The average output power after mixing the pump and signal from two branches of the same oscillator in a nonlinear crystal, MgO:$LiNbO_3$, is 1.1 mW at 3.6 μm [18]. Nevertheless, at almost the same wavelength, 3.2 μm, Tyler W. Neely *et al.* got 128 mW. Such results were accomplished by mixing the pump and signal from an Yb:fiber oscillator in MgO:PPLN crystal [19]. The distinct point here in comparison with [17, 18] is that the signal is a Raman shifted soliton which is generated in a zero-dispersion wavelength photonic crystal fiber (PCF) while the pump is a chirped amplified pulse. One year after [19] published their results, a tunable frequency comb ranging from 3 to 10 μm from Yb:fiber laser was achieved in a GaSe crystal with an average power of 1.5 mW [11]. Similar to the idea of [19], in [11], the signal is also a Raman shifted soliton but it was formed in a suspended-core fiber. In almost the same spectral range, 5 to 12 μm , Alessio Gambetta *et al.* gained approximately 100 μW in a 1 mm GaSe from a two-branch Er:fiber laser producing 65 fs centered at 1.55 μm with a 100 MHz stabilized repetition rate [20].

In the longer range of the fingerprint, R. A. Kaindl generated a wide range of MIR, 9-18 μm, in a 1mm GaSe from a 20 fs broadband Ti:Sapphire laser at a repetition rate of 88 MHz centered at 830 nm. The average power measured is around 1μW and the MIR pulse width is nearly 140 fs [14]. A very wide tunable range of MIR, 4 to 17 μm, was achieved by mixing pulses coming from a 100 fs Er:fiber laser centered at 1.55 μm and their supercontinuum (SC) in the 1.7-2.3 μm region in a 1 mm GaSe crystal. The output power obtained was 1 mW [15]. Long wavelengths of the fingerprint region were also achieved when using Yb:fiber lasers. In particular, 20 μW of a MIR at 18 μm was generated by mixing 300 mW of two-color signals into a GaSe crystal. The Yb:fiber oscillator generates

200 fs pulses at a repetition rate of 50 MHz [21]. The longest MIR wavelength, up to 20 μm, was achieved by [16, 22]. The pump and signal were synthesized in an Yb:fiber CPA system. 30 μW of average power at 18 μm was obtained by mixing around 1.4 W of the pump and signal in a 1 mm GaSe crystal.

1.3 Outline of The Thesis

This thesis is composed of 5 sections: introduction, background, experimental setup, experimental results and discussion and conclusion.

Section 2 focuses on theoretical background of this thesis. The theory of chirped pulse amplification technique will be discussed. Particularly, group velocity dispersion, pulse stretcher and compressor will be investigated. The mechanism of amplification occurring in Yb:fiber amplifiers will be addressed. Next, we will discuss about timing jitter of Yb:fiber lasers. Interferometric and non-collinear intensity cross correlation will be covered in this section. Finally, the method and non-linear crystal used to generate MIR, DFG and GaSe, will be studied. Finally, we will briefly mention about a SC generation tool and chirped fiber Bragg gratings.

In section 3, the whole experimental setup will be described and explained in details. The whole setup is separated into smaller parts: CPA, MIR generation and timing jitter measurement.

Section 4 will present the experimental results achieved including SC generation, two-color signal generation, CPA, MIR generation and jitter measurement. Then, we will discuss about the results we obtained.

Finally, section 5 is about conclusion.

2 Background

2.1 Chirped Pulse Amplification

2.1.1 Introduction

Chirped pulse amplification technique, usually called CPA for short, was invented in 1985 by D Strickland and G Mourou [23]. The purpose of this greatly useful technique is to prevent intensity of amplified pulses from reaching damage threshold of amplification media. Such amplified pulses with high peak power may cause damage to the amplifiers due to optical Kerr lensing effect. This effect is based on dependence of refractive index n of the amplification materials on the pulse's intensity $I(t)$

$$n = n_0 + n_2 I(t) \tag{6}$$

where n_2 is nonlinear index of refraction, it depends on the materials but mostly it is often positive [24]. Kerr lensing effect can occur in most of optical materials. When an intense beam propagates in an optical medium with $n_2 > 0$, its higher intensity in the center results in a steep rise in the refractive index in the beam center. This turns out that the medium works like a positive nonlinear lens to change the beam radius as is illustrated by Figure 2.1 [25]. This induced effect is called self-focusing effect. Finally, the resultant self-focused beam can definitely damage the optical medium [24]. This can be avoided by employing CPA technique.

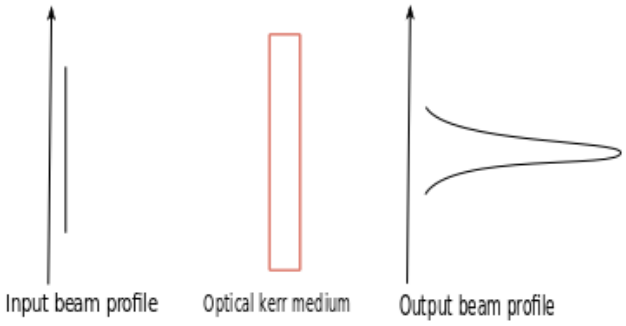

Figure 2.1: Self-focusing beam in optical Kerr medium [25]

The CPA employs the idea of temporal dispersion. This concept will be explained in section 2.1.2. A brief explanation is that initially unchirped pulses are made temporally chirped before being amplified without changing the corresponding spectrum. Generally,

the electric field of ultrashort pulses have time-dependent amplitude and phase. So the equation (1) should be written in its general form as

$$E(t) = A(t)\, e^{\imath\phi(t)} \tag{7}$$

The angular frequency is defined as

$$\omega(t) \equiv \frac{d\phi}{dt} \tag{8}$$

For an unchirped pulse, the phase $\phi(t)$ is a linear function of time $\phi(t) = \phi_0 + \omega_0 t$, hence equation (7) has the form of equation (1), and the frequency is ω_0 which is a constant along the pulse. Figure 2.2 shows an unchirped Gaussian pulse with a constant frequency along the pulse. However, when the pulse is made linearly chirped, its temporal phase no longer depends on time linearly but quadratically. Let us assume that it has the form of $\phi(t) = \phi_0 + \omega_0 t + bt^2$ where b is some coefficient. In that case, the angular frequency is not a constant with respect to time, but is linearly dependent on time $\omega(t) = \omega_0 + bt$. If this instantaneous frequency increases, the pulse is positively chirped. Otherwise, the pulse is negatively chirped.

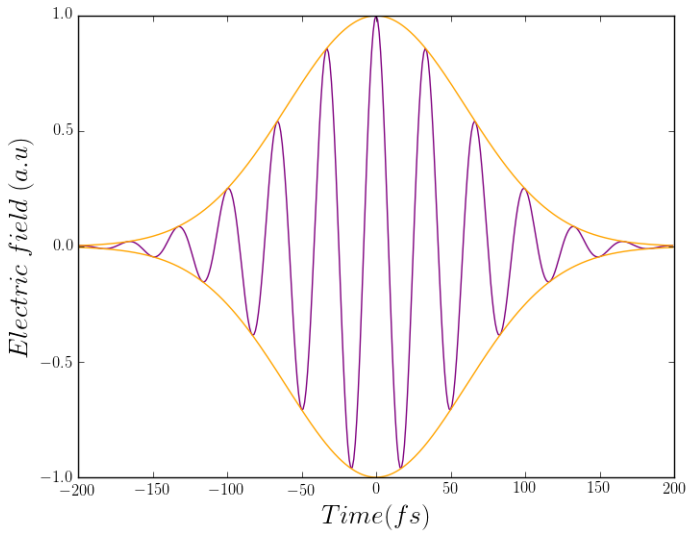

Figure 2.2: An unchirped Gaussian pulse

The CPA technique is illustrated briefly by Figure 2.3. A CPA system contains three main parts: stretchers, amplifiers and compressors. Each part will be described in details in the following sections. According to this technique, first of all, pulses have to be stretched in a dispersive system to decrease their peak power. Next, they can be safely amplified.

Finally, the amplified and stretched pulses are compressed back to their initial pulse-width, ideally, by passing through another dispersive system of which the dispersion sign has to be opposite to that of the stretchers [24].

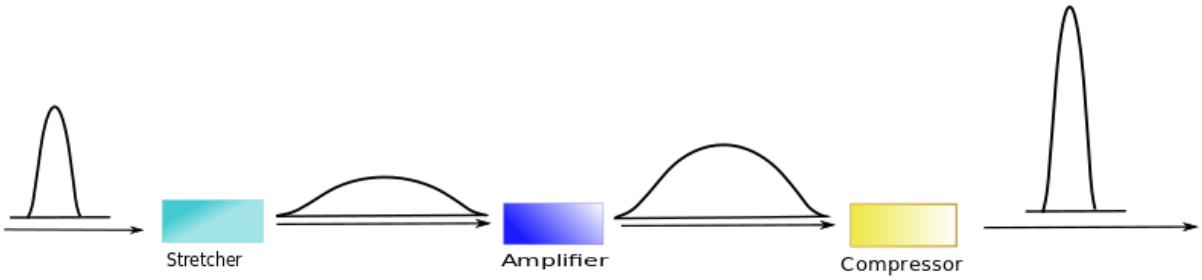

Figure 2.3: Sketch of CPA technique

2.1.2 Group Velocity Dispersion

When a pulse propagates through a dispersive medium of length L, it experiences a spectral phase $\phi(\omega)$. Assuming that the input pulse's spectrum is $E_{in}(\omega)$ then the output pulse in the time domain can be written as

$$E_{out}(t) = \frac{1}{2\pi} \int d\omega E_{in}(\omega) e^{\imath[\omega t + \phi(\omega)]} \tag{9}$$

where the phase

$$\phi(\omega) = -\beta(\omega) L \tag{10}$$

depends on the propagation constant of the medium defined as

$$\beta(\omega) = \frac{\omega n(\omega)}{c} \tag{11}$$

The phase can be Taylor series expanded at the central frequency ω_0 as

$$\phi(\omega) = \phi_0 + (\omega - \omega_0)\phi_1 + \frac{1}{2}(\omega - \omega_0)^2 \phi_2 + \frac{1}{6}(\omega - \omega_0)^3 \phi_3 + \cdots \tag{12}$$

where $\phi_n = \left(\frac{\partial^n \phi}{\partial \omega^n}\right)_{\omega_0}$, specifically ϕ_0 is absolute phase while ϕ_1, ϕ_2, ϕ_3 are known as group delay, second-order dispersion (SOD) or group delay dispersion denoted as GDD, third-order dispersion (TOD), respectively. Non-zero ϕ_2 is equivalent to a linearly chirped pulse while non-zero ϕ_3 is corresponding to a quadratically chirped pulse. To have a better and clearer understanding about the concept of 'chirp', let us discuss how a dispersive medium

impacts a pulse. First of all, equation (12) can be rewritten in terms of $\beta(\omega)$ as

$$\begin{aligned}\beta(\omega) &= \beta(\omega_0) + \frac{\partial\beta}{\partial\omega}|_{\omega_0}(\omega-\omega_0) + \frac{1}{2}\frac{\partial^2\beta}{\partial\omega^2}|_{\omega_0}(\omega-\omega_0)^2 + \frac{1}{6}\frac{\partial^3\beta}{\partial\omega^3}|_{\omega_0}(\omega-\omega_0)^3 + \cdots \\ &= \beta_0 + \beta_1(\omega-\omega_0) + \frac{\beta_2}{2}(\omega-\omega_0)^2 + \frac{\beta_3}{6}(\omega-\omega_0)^3 + \cdots \end{aligned} \tag{13}$$

where $\beta_n = \left(\frac{\partial^n\beta}{\partial\omega^n}\right)_{\omega_0}$.
Next, we insert equation (13) into equation (9) and rearrange it in such a way that the pulse's electric field can be composed of two separate parts: carrier term which is independent on ω, $e^{\imath(\omega_0 t-\beta_0 L)}$, and envelope function $a_{out}(t)$, specifically

$$E_{out}(t) = Re\left\{e^{\imath(\omega_0 t-\beta_0 L)}a_{out}(t)\right\} \tag{14}$$

$$a_{out}(t) = \frac{1}{2\pi}\int d\tilde{\omega}A(\tilde{\omega})\,e^{\imath\left[\tilde{\omega}t-\left\{\beta_1\tilde{\omega}+\frac{\beta_2}{2}\tilde{\omega}^2+\cdots\right\}L\right]} \tag{15}$$

and

$$\tilde{\omega} = \omega - \omega_0 \tag{16}$$

This expression shows that the variation of β with respect to ω does not influence the carrier term, and that the carrier term propagates at the phase velocity $v_{ph} = \frac{\omega_0}{\beta_0}$, and that this variation only affects the envelope. In particular, if the pulse propagates in such a medium that $\beta(\omega)$ depends on frequency linearly:

$$\beta(\omega) = \beta_0 + \beta_1\tilde{\omega} \tag{17}$$

then the envelope of the output pulse becomes

$$a_{out}(t) = a_{in}(t-\beta_1 L) \tag{18}$$

Therefore, it is obvious that the output pulse is exactly a copy of the input pulse and travels at the group velocity, $v_g = \beta_1^{-1}$. In other words, the dispersive medium determines the group velocity and, hence, the time duration that a pulse needs to pass through that medium. The time duration or group delay is given by the second term of equation (18). That is

$$\tau = \beta_1 L = \frac{L}{v_g} \tag{19}$$

However, if $\beta(\omega)$ does not depend on frequency linearly, then the output pulse is no longer identical to the input pulse. The variation in group delay with respect to frequency is given

by

$$\begin{aligned}\Delta\tau(\omega) &= \tau(\omega) - \tau(\omega_0) = (\omega - \omega_0)\frac{\partial\tau}{\partial\omega} \\ &= (\omega - \omega_0)\beta_2 L \end{aligned} \tag{20}$$

This equation can also be generalized to determine the chirp amount of a pulse with a spectrum bandwidth of $\Delta\omega$ as [24]

$$\Delta\tau(\omega) = \beta_2 L \cdot \Delta\omega \tag{21}$$

or by substituting equation (11) into (21), the chirp amount is equivalent to

$$\Delta\tau(\omega) = \frac{\lambda^3 L}{2\pi c^2}\frac{d^2 n}{d\lambda^2}\Delta\omega \tag{22}$$

If the GDD, $\beta_2 L$, is positive then the dispersion is positive otherwise it is negative.

The concept of GDD is very important in a CPA system. It is considered to be a guideline to set up the system practically because it is very important for SOD and TOD in- stretchers, all materials and compressors to be compensated simultaneously [26], i.e.

$$\phi_2^{stretcher} + \phi_2^{material} + \phi_2^{compressor} = 0 \tag{23}$$

$$\phi_3^{stretcher} + \phi_3^{material} + \phi_3^{compressor} = 0 \tag{24}$$

In practice, there are several ways to make a pulse temporally chirped. That can be using material dispersion where $n = n(\lambda)$. Optical fibers are popularly used due to this reason. In addition, using angular or geometrical dispersion, such as prisms and gratings, is another option.

2.1.3 Ultrashort Pulse Stretcher

Generally, a pulse can be stretched in a positive GDD medium such as grating stretchers and fibers. In fiber optics, it is popular that the SOD and TOD can be written in terms of wavelength λ as given by equations [24]

$$\Delta\tau(\lambda) = -\frac{2\pi c\beta_2 \Delta\lambda L}{\lambda^2} \tag{25}$$

This can be rewritten in terms of– dispersion parameter D(ps nm^{-1} km^{-1}) defined as

$$D = -\frac{\lambda}{c}\frac{d^2n}{d\lambda^2} \tag{26}$$

$$\Delta\tau\left(\lambda\right) = DL\Delta\lambda \tag{27}$$

Accordingly, SOD and TOD become [24]

$$\phi_2 = -\frac{\lambda^3 L}{2\pi c^2}\frac{d^2n}{d\lambda^2} \tag{28}$$

$$\phi_3 = \frac{\lambda^4 L}{4\pi^2 c^3}\left[3\frac{d^2n}{d\lambda^2} + \lambda\frac{d^3n}{d\lambda^3}\right] \tag{29}$$

In this thesis, silica fiber was used for pulse stretching because of the fact that index of refraction of this fiber depends on wavelength as shown in equation (30) [27]. Obviously, all equations above, (25 - 29) can be applied.

$$n\left(\lambda\right) = 1.4508554 - 0.0031268\lambda^2 - 0.0000381\lambda^4 + \frac{0.0030270}{\lambda^2 - 0.035} - \frac{0.0000779}{\left(\lambda^2 - 0.035\right)^2} + \frac{0.0000018}{\left(\lambda^2 - 0.035\right)^3} \tag{30}$$

2.1.4 Ytterbium Doped Fiber Amplifiers

Rare earth ions are doped in a fiber's core which has higher refractive index than its cladding so that amplified signals can propagate in the core due to total internal reflection. There are a few advantages that Yb:fiber amplifiers have over other rare earth doped fibers. The first advantage is that they can give very high output power. In addition, their amplification bandwidth is broad, in particular from 975 to 1200 nm. Finally, they accept a broad pumping bandwidth as well, between 860 and 1064 nm, which brings more options of pumping schemes to fiber users [28].

The mechanism of the amplification in fibers is similar to that happening in an regular laser. This means that stimulated emission is the key point. In other words, when a fiber is pumped, its dopant ions initially at ground states are excited to higher energy levels or excited states. These ions can decay spontaneously and release photons of which the energy is equal to energy difference of the two levels. Moreover, the emitted photons from different atoms have no phase relation with each other and travel in any directions. This process is called spontaneous emission (left diagram of Figure 2.4). Amplified spontaneous emission (ASE) is generated in pumped fibers via this mechanism. It exists in the fibers

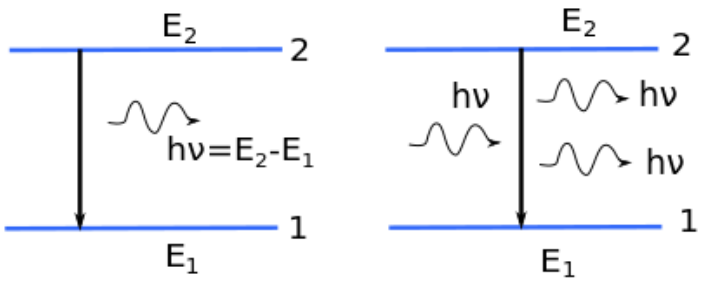

Figure 2.4: Left: Spontaneous emission - Right: Stimulated emission

regardless of the fact that the pumped fibers are seeded or not. Generally, it is an unwanted and unavoidable effect or noise in fiber amplifiers. However, it definitely can be decreased significantly or even precluded relying on many other factors such as fiber length, fiber type (i.e. single clad or double clad), pump and seed power. Nevertheless, if the fiber is seeded by a signal with some known frequency, photons are still emitted but they, all, together with the signal are in phase. Furthermore, all of the photons travel in the same direction. This is called stimulated emission (right diagram of Figure 2.4). As a result, the signal is amplified through this phenomenon [29].

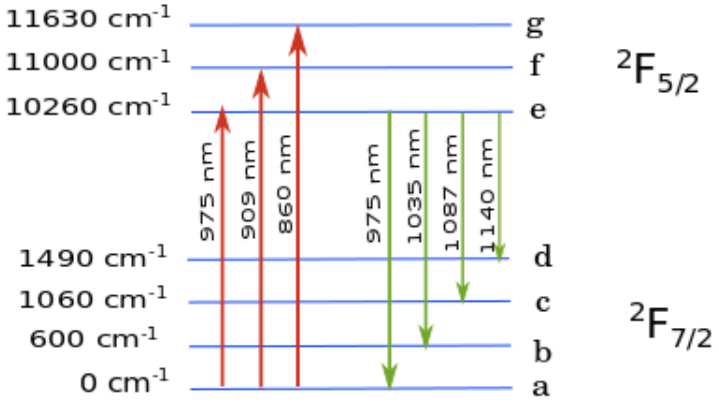

Figure 2.5: Energy level structure of Yb^{3+} [30]

In order that the signal can be highly amplified in Yb:fibers, a proper combination of pumping and signal wavelengths should be carefully investigated. As a result, it is helpful to discuss about the energy level structure as well as the absorption and emission cross section of Yb^{3+}. There are two manifolds in the Yb^{3+} energy level structure: ground manifold $^2F_{7/2}$ and excited manifold $^2F_{5/2}$. Each manifold consists of several sub-levels. Figure 2.5 shows that the ground manifold contains sub-levels a, b, c, d while the excited

manifold has three sub-levels e, f and g. The absorption and emission cross section of Yb^{3+} is shown in Figure 1b of [30].

As is shown by Figure 2.5, if the ions are pumped at 975, 909 and 860 nm, they will be excited and transit from sub-level a in the ground manifold to sub-level e, f, g, respectively. As the excited ions at sub-levels f, g are not stable, they start to decay to sub-level e and then transit to the ground manifold at different wavelengths shown in green lines. Depending on the wavelengths of the seed signals, pump wavelengths can be chosen properly. That is why the absorption and emission cross sections described in Figure 1b of [30] are useful. In accordance with that graph, there are two peaks of absorption, at 910 and 975 nm, and two peaks of emission at 975 and 1030 nm. For high amplification efficiency, the wavelength of the pump should be as close as possible to the peaks of absorption while the signal wavelength that needs to be amplified should be close to or at the emission peaks. Therefore, there are two best options for the pump wavelength. Firstly, if the fiber is pumped at around 910 nm, the gain obtained at 975 nm will be higher than the gain at 1035, 1087 and 1140 nm because the emission cross section at 975 nm is the highest according to Figure 1b of [30]. Thus, this is consistent with the energy level structure in Figure 2.5. If the pump wavelength is 975 nm, the gain at the long wavelength range, 1000 to 1150 nm, in the Figure 1b will be achieved because their emission cross sections are much higher than their absorption cross sections. Besides, one remarkable point is that the absorption bandwidth at 975 nm is very narrow. Thus, the pump bandwidth should be narrow as well. In this thesis, the two amplified signal wavelengths are 1025 and 1085 nm. Consequently, a diode-laser pump at 975 nm was used instead of at 910 nm to avoid strong ASE which is the gain at around 975 nm.

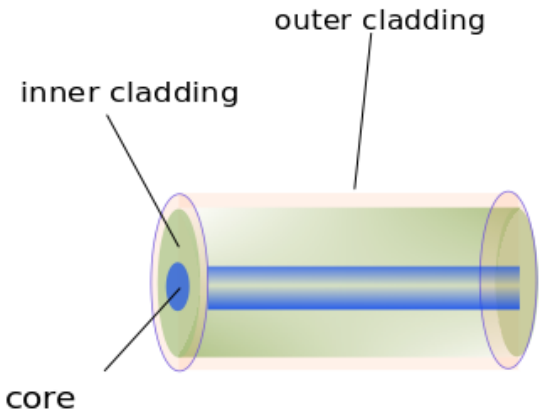

Figure 2.6: A double-clad fiber

In this thesis, double-clad fibers, as is illustrated by Figure 2.6, were used in all of the amplification stages because they can support the multi-mode pumps. In terms of pumping schemes, there are two schemes basically. They are core and cladding pumping. In the former, both of the pump and the fiber are single-mode and the pump does the pumping in the core of the fiber. In the latter, the pump is multi-mode while remaining the output signal to be single-mode if the input is single-mode. In addition, the pump light is coupled into the fiber's inner cladding which has higher refractive index than the outer cladding. Hence, the pump light can travel along the fiber via total internal reflection. When the pump beam crosses the core, it amplifies the signal traveling in the core. In this thesis, cladding pumping was preferable due to high output power and high pumping power.

2.1.5 Ultrashort Pulse Compressor

The compressor used in this thesis is Treacy's grating setup. It consists of two typical transmission gratings. They should be aligned to be parallel to each other. According to this setup, the SOD or GDD can cancel the positive GDD produced in the grating stretcher and materials if the incident angle θ_i of the pulses, grating period d and the distance between the two gratings, namely compressor length L, are properly chosen. Particularly, GDD is given by [29] [31]

$$\phi_2 = \frac{-\lambda_0^3 L}{\pi c^2 d^2 \left[1 - \left(\frac{\lambda_0}{d} - \sin\theta_i\right)^2\right]^{3/2}} \tag{31}$$

where λ_0 is the wavelength of the light.
The minus sign in front of equation (31) indicates that the grating compressor always give negative GDD on the pulses. Consequently, this can be considered as its main advantage. Besides, in systems that different wavelengths need to be spatially separated then the grating compressor is a good choice. However, one disadvantage of the grating compressor is that it cannot cancel TOD generated in materials including fiber stretchers, fiber amplifiers because both of its TOD and the materials' TOD are positive [26]. Note that the space between the two gratings do not contribute to the GDD of the pulses.

2.2 Timing Jitter of Yb:fiber Laser

2.2.1 Introduction

Since the femtosecond pulses were generated for the first time in optical fiber lasers in 1990, ultrafast fiber lasers have been developed significantly and contributing to the development of frequency metrology. Therefore, many researches have been focusing on

stabilizing the lasers including reducing the noises. Fiber lasers have the smallest timing jitter in comparison with bulk and semiconductor lasers [32]. Moreover, such systems can provide not only short pulses but also high output power so they definitely can compete with other laser systems. Especially, fiber lasers have one advantage over Ti:sapphire lasers, which is its compact size. Although fiber laser systems based on rare-earth doped fibers such as Yb^{3+}, Er^{3+}, -Yb^{3+} and Nd^{3+} have been grown, the systems based on Yb are most widely used because they can offer a wide bandwidth, high efficiency of conversion and long time of energy storage [33].

There are many factors that can contribute to the fluctuation of the repetition rate of a mode-locked fiber laser. In general, they can be any fluctuation in the cavity length and laser pump, ASE and acoustic interactions in the fiber. Amongst these, the cavity-length fluctuation and ASE are the candidates causing the jitter the most compared to the negligible pump fluctuation and acoustic interactions. Technically, the length of the cavity depends dramatically on temperature. It is because in fiber lasers, the refractive index n of the fiber relies on temperature T. For instance, in silica, $\frac{\partial n}{\partial T} = 1.1 \times 10^{-5}$, if the temperature changes by 1^oC then the optical path length of 1 m fiber is changed by 11 μm [32].

Recently, many methods have been built and applied to measure the laser's timing jitter. The two well-known methods are optical cross correlation and radio frequency (RF) electrical spectrum [34]-[38]. It was shown that the two methods give close results [35]. In this thesis, the optical cross correlation method was used to measure the time fluctuation from pulse to pulse. In our experiment, a testing-alignment step had been performed first by employing the interferometric autocorrelation. The goal was to find out if the alignment in the setup was properly set up and if the stability of the optical devices was good. Then, the jitter was measured in time domain by using the optical cross correlation.

2.2.2 Interferometric Autocorrelation

An input beam is split into two by a beam splitter and then each beam propagates along two different arms as shown in Figure 2.7. This setup employs the Michelson interferometry technique. One pulse is delayed by τ with respect to the other. The electric fields of the pulses from those arms after the interferometer and before the second harmonic generation (SHG) crystal are $E(t)$ and $E(t-\tau)$. The output field and intensity as a function of the time delay τ on a SHG crystal are given by [39]

$$E(\tau) = E(t) + E(t-\tau) \tag{32}$$

and

$$\begin{aligned} I(\tau) &= \int_{-\infty}^{\infty} \left|\left[E(t) + E(t-\tau)\right]^2\right|^2 dt \\ &= \int_{-\infty}^{\infty} \left|E^2(t) + 2E(t)\,E(t-\tau) + E^2(t-\tau)\right|^2 dt \end{aligned} \tag{33}$$

Equation (33) above can be expanded as

$$\begin{aligned} I(\tau) &= \int_{-\infty}^{\infty} \left\{I(t)^2 + I(t-\tau)^2\right\} dt \\ &\quad +2\int_{-\infty}^{\infty} \left\{I(t) + I(t-\tau)\right\} \mathrm{Re}\left\{E(t)\,E^*(t-\tau)\right\} dt + c.c \\ &\quad +\int \mathrm{Re}\left\{E(t)^2\,E^*(t-\tau)^2\right\} dt + c.c \\ &\quad +4\int_{-\infty}^{\infty} I(t)\,I(t-\tau)\,dt \end{aligned} \tag{34}$$

The first term is simply an addition of the two intensities. It is a constant, so called background, while the last term is from non-collinear autocorrelation (this will be discussed in section 2.2.3). Only the two crossing terms and their conjugates in the middle of the equation contribute to the interferogram. Note that the intensity of the pulse is expressed as

$$I(t) = E(t)\,E^*(t) \tag{35}$$

and that the electric field of the pulse contains the envelope part (complex amplitude $A(t)$) and the carrier part

$$E(t) = A(t)\,e^{\imath(\omega_0 t + \phi_{CE})}. \tag{36}$$

Substituting (36) into (34), it is obvious that the second term in (34) is a coherence term which oscillates at a frequency of ω_0 while the third term oscillates at $2\omega_0$.

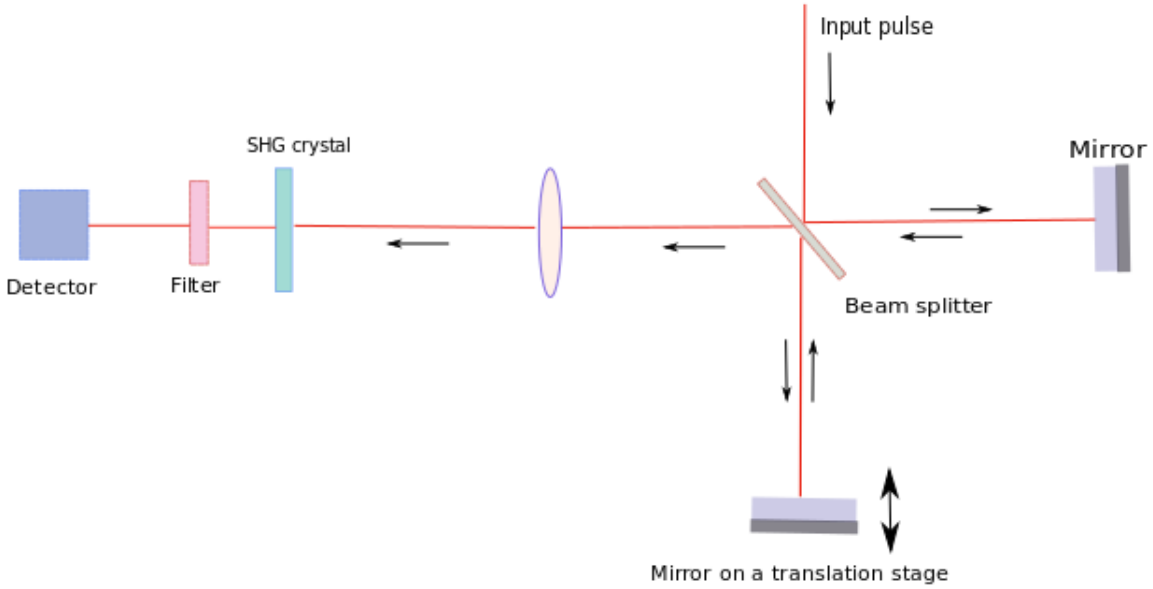

Figure 2.7: Sketch of interferometric autocorrelation

At zero time delay, each term becomes

$$I_{background}\left(\tau=0\right)=2\int_{-\infty}^{\infty}I\left(t\right)^{2}dt \tag{37}$$

$$I_{\omega_0}\left(\tau=0\right)=8\int_{-\infty}^{\infty}I\left(t\right)^{2}dt=4I_{background} \tag{38}$$

$$I_{2\omega_0}\left(\tau=0\right)=2\int_{-\infty}^{\infty}I\left(t\right)^{2}dt=I_{background} \tag{39}$$

$$I_{autocorrelation}=2I_{background} \tag{40}$$

It means that– [39]

$$\frac{I\left(\tau=0\right)}{I_{background}}=8 \tag{41}$$

The ratio shown in equation (41) can be achieved if the alignment is good, stable and phase matching conditions of the SHG crystal are satisfied. Moreover, in general, the fringes in all cases have to be symmetric because $I\left(\tau\right)=I\left(-\tau\right)$.

2.2.3 Non-collinear Intensity Autocorrelation

Similarly to the case of interferometric autocorrelation discussed above, the beam is also split into two as is shown by Figure 2.8. However, in this case, there is no background

overlapping with the generated second harmonic light. So the only term achieved will be [39]

$$I_{autocorrelation} = \int_{-\infty}^{\infty} I(t)\, I(t-\tau)\, dt \tag{42}$$

The autocorrelation pulse should be symmetric, similar to the interferometric fringes, because $I(\tau) = I(-\tau)$.

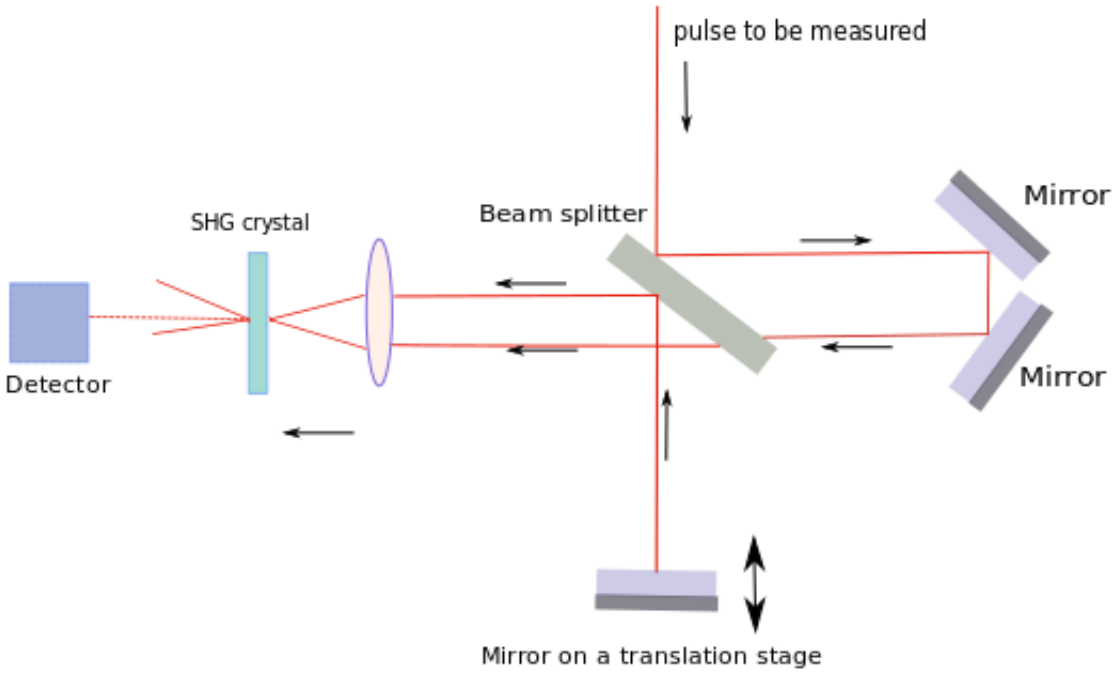

Figure 2.8: Sketch of the setup of the non-collinear autocorrelation

2.2.4 Timing Jitter Measurement based on Optical Cross Correlation

In the optical cross correlation technique used to measure the timing jitter, the setup is similar to that of the non-collinear intensity autocorrelation. The timing jitter of Gaussian pulses is given by [34]

$$\tau_{jitter}^2 = \tau_{CC}^2 - \tau_{AC}^2 \tag{43}$$

where τ_{jitter} is the timing jitter, τ_{CC} is the full width at half maximum (FWHM) of the cross correlation and τ_{AC} is the FWHM of the autocorrelation.

The FWHM of the autocorrelation is achieved when the difference in the optical path length ΔL between the two arms is less than a pulse-width. In the case of the cross correlation, ΔL can be $N.T_{RT}$, where N is a positive integer and $N \geq 1$. It means that

the second harmonic is generated between two different pulses. In this thesis, the cross correlation was performed between two adjacent pulses or $N = 1$.

2.3 Ultrafast Mid-infrared Generation based on Difference Frequency Generation

2.3.1 Difference Frequency Generation

Difference frequency generation is a down frequency conversion process. This second-order non-linear process is illustrated by Figure 2.9. Conventionally, in the DFG technique, the pump denoted as ω_p is the highest frequency, the idler ω_i is the lowest frequency and ω_s is called the signal [40].

$$\omega_i = \omega_p - \omega_s \tag{44}$$

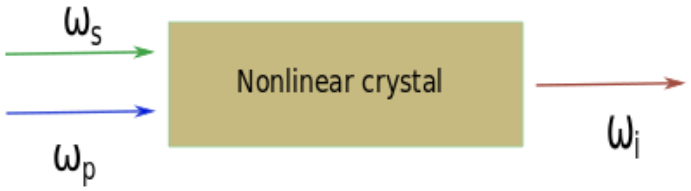

Figure 2.9: Schematic diagram of DFG

The phase mismatch Δk in a nonlinear crystal is given by

$$\Delta k = k_p - k_s - k_i \tag{45}$$

where k_p, k_s, k_i are the wave vectors of the pump, signal and idler and

$$k = n\omega/c \tag{46}$$

The generalized phase matching condition is given by

$$\Delta k = 0 \tag{47}$$

or

$$n_i\omega_i = n_p\omega_p - n_s\omega_s \tag{48}$$

The idler intensity is a function of the product of the pump and signal intensity, $I_p I_s$ [40]

$$I_{DFG} = \frac{2\omega_i^2 d_{eff}^2 L^2 I_p I_s}{c^3 \epsilon_0 n_p n_s n_i} \tag{49}$$

In this equation, ϵ_0 is the dielectric constant and n_p, n_s, n_i are refractive indices of the pump, signal and idler, c is the vacuum wavelength, L is the interaction length, d_{eff} is the effective nonlinear coefficient.

2.3.2 Gallium Selenide

In this thesis, the GaSe crystal was used for the MIR generation. Its transparency range is from 0.62 to 20 μm. In addition, this is a negative uniaxial and birefringent crystal. Its refractive index depends on the polarization direction of the light beams.

In the GaSe crystal, it is suggested that the pump's polarization should be orthogonal to the polarization of the signal to increase the conversion efficiency. Specifically, in this thesis, the pump is set to be e-polarized while the signal has o-polarization. When a light beam's polarization direction is in the same plane with a plane formed by its wave vector $\vec{k}$ and the optic axis $\hat{c}$ of the crystal, its polarization is called extraordinary polarized (e-polarized for short) or p-polarized. On the other hand, if the direction of the light's polarization is perpendicular to that plane then it has ordinary polarization (o-polarized for short) or s-polarized. Depending on the polarization of the output beam ω_i, the phase matching types in GaSe are classified into two different types. In type I (eoo), the phase matching is

$$n_i^o \omega_i = n_p^e \omega_p - n_s^o \omega_s \tag{50}$$

and type II phase matching (eoe) is given by

$$n_i^e \omega_i = n_p^e \omega_p - n_s^o \omega_s \tag{51}$$

Generally, the phase matching condition can be fulfilled by angle tuning, temperature tuning or wavelength tuning. In the case of GaSe, its phase matching condition is obtained by angle tuning. It is because of the fact that depending on the beam's incident angle θ between $\vec{k}$ and $\hat{c}$, the beam can experience different refractive index [40], i.e.,

$$\frac{1}{n_e(\theta)^2} = \frac{\sin^2\theta}{\bar{n}_e^2} + \frac{\cos^2\theta}{n_o^2} \tag{52}$$

In this equation, $n_e(\theta)$ is the refractive index of the e-beam, $\bar{n}_e$ is called principle value of the extraordinary refractive index and n_o is ordinary refractive index. If $\theta = 90^0$ then

$n_e = \bar{n}_e$ and if $\theta = 0^0$ then $n_e = n_o$. As a result, the phase matching condition is satisfied by combining the equation (50), (51) and (52) to find the phase matching angle θ.

Once the phase matching angle θ is found, the conversion efficiency can be dramatically optimized because it relies on both of the interaction length L of the crystal and d_{eff}. The interaction length is often called the walk-off distance or aperture length. In other words, the three beams have different frequencies and different polarizations. So, technically, they just travel together or spatially overlap in the crystal for a certain distance after which they start separating from each other. It means that the conversion efficiency can be dramatically increased if the walk-off distance is the same as the crystal length to ensure that once they still travel in the crystal, they overlap in space. Consequently, it is necessary to find the walk-off distance L given by [40]

$$L = \frac{\sqrt{\pi}}{\rho} w_o \tag{53}$$

where w_o is the 1/e power radius of the Gaussian beam of the idler or the signal and ρ is the walk-off angle which depends on the phase matching angle θ as below [41]

$$\rho = -\frac{1}{n_e} \cdot \frac{dn_e}{d\theta} \tag{54}$$

Furthermore, the effective second-order coefficient d_{eff} of the GaSe crystal corresponding to a certain phase matching type is given by [42]

$$d_{eoo} = d_{22} \cos\theta \sin 3\phi \tag{55}$$

and

$$d_{eoe} = d_{22} \cos^2\theta \cos 3\phi \tag{56}$$

d_{22} is the second-order nonlinear coefficient which is equal to 54 pm/V. In order to increase the conversion efficiency, not only the angle θ but also the azimuthal angle ϕ are important.

2.4 Super-continuum Generation

The PCF for generating a SC has a solid core made of glass in the center. The core is surrounded by a cladding consisting of an array of air holes along the longitudinal central axis of the fiber. Moreover, for this type of PCF, the fraction of the air-fill areas is larger than that of core areas. In addition, the cladding has lower refractive index than the glass core. So, total internal reflection is the phenomenon guiding pulses traveling in the core like standard fibers. In femtosecond regime, SC generation in the PCF is caused by not only high nonlinear effects, such as self phase modulation (SPM), cross phase modulation,

soliton effects, Raman scattering, modulation instability and four-wave mixing, but also dispersion properties of the PCF with respect to the incident wavelengths. The former is the key for generating SC for low energy pulses (nanojoules like our case). When the SC is generated, it means that the narrow bandwidth of the incident pulses is broadened after propagating through the PCF [43] [44]. A bandwidth can be spanned more than an octave. Our SC is an example (see Figure 4.2 for the SC and Figure 4.1 for the input).

Generally, a combination between femtosecond pulses and an anomalous group velocity dispersion (GVD) regime close to the zero-dispersion wavelength of the PCF can generate a very broad (white light) spectrum. We switched from such PCF to all-normal dispersion (AND) PCF. Our current PCF's dispersion is normal and flat in the range of 1000-1100 nm. The zero-dispersion PCF is not stable due to soliton effects generating the SC, whereas, AND PCF generates a SC in such a way that the soliton formation is precluded while the SPM is dominated. The SPM can ensure that the input pulse coherence can be preserved, thus the output is more spectrally stable, which is not the case for the zero-dispersion PCF [45].

2.5 Chirped Fiber Bragg Gratings

A normal fiber has a uniform refractive index along its length. In fiber Bragg gratings (FBGs), the refractive index of the fiber core changes periodically or aperiodically along a short length. Such refractive index perturbation makes the FBGs work like spectral filters which can reflect a narrow wavelength range and transmit other wavelengths. In principle, a uniform period FBGs employ the Bragg effect to reflect a light:

$$\lambda_{Bragg} = 2n_{eff}\Lambda \tag{57}$$

where Λ is the period of the grating, n_{eff} is the effective refractive index for light propagating in the core and λ_{Bragg} is the centered wavelength of the narrow reflected bandwidth, called Bragg wavelength. In general, if a light beam containing a range of wavelengths is launched into a FBG, the wavelengths that are in phase with the grating's period will be reflected back to the input end while those are not in phase with the period will pass through the FBG [46]. In a chirped fiber Bragg grating (CFBG), the grating's period is non-uniform along its length. If the period changes linearly with the grating's length then the chirp induced in the grating is linear. There are many applications of CFBGs. They can be used to correct and compensate dispersion, suppress ASE, flatten gain of an amplifier. They can also be used in a CPA or as in-fiber band-pass filters, etc [47]. [47].

3 Experimental Setup

The long-term goal of this research is to make a frequency comb at a long wavelength of around 18 μm. Towards this goal, this thesis project had two main experimental tasks. The first task is to generate MIR based on DFG, and the second one is to test whether the cavity length of the Yb:fiber laser is sufficiently stable so that a frequency comb can be realized by difference frequency mixing. Otherwise, active stabilization will be required, which is beyond the current thesis project. The sketch of our complete experimental system is shown in Figure 3.1.

Details of the CPA system developed as a part of this thesis have been published in [48] and are given in section 3.1. The experimental setup for the MIR generation was the same as [16]. The timing jitter measurement of the Yb:fiber laser was based on the setup used in [49]. In this case, the cross correlation technique with background-free was applied.

The CPA setup used in this thesis as well as in [48] largely modified the setup used in [16] to increase output efficiency, system stability and apparatus compactness. Commonalities between the two setups include an ultrashort Yb:fiber laser, a PCF to make a SC, two amplification stages, a fiber stretcher, and a grating compressor. Modifications to the setup used in [16] include a AND PCF, a CFBG for two-color selection replacing the notch filter, removal of grating stretcher and, most importantly, splicing fibers.

In the MIR generation setup, the two color wavelengths were down-frequency mixed in the same GaSe crystal as in [16]. Lenses with different focal lengths were used to focus the signals on the GaSe crystal to optimize the output MIR power. In addition, the process of MIR detection was performed by different setups and measured by two devices. The first device was HgCdTe (Mercury Cadmium Telluride or MCT) as in [16], and the second device was thermal detector for average power measurement. This will be discussed further in section 3.2.

Section 3.3, describes details of cross-correlator technique used for measuring timing jitter. This setup is to measure the autocorrelation width and the cross correlation width of adjacent pulses.

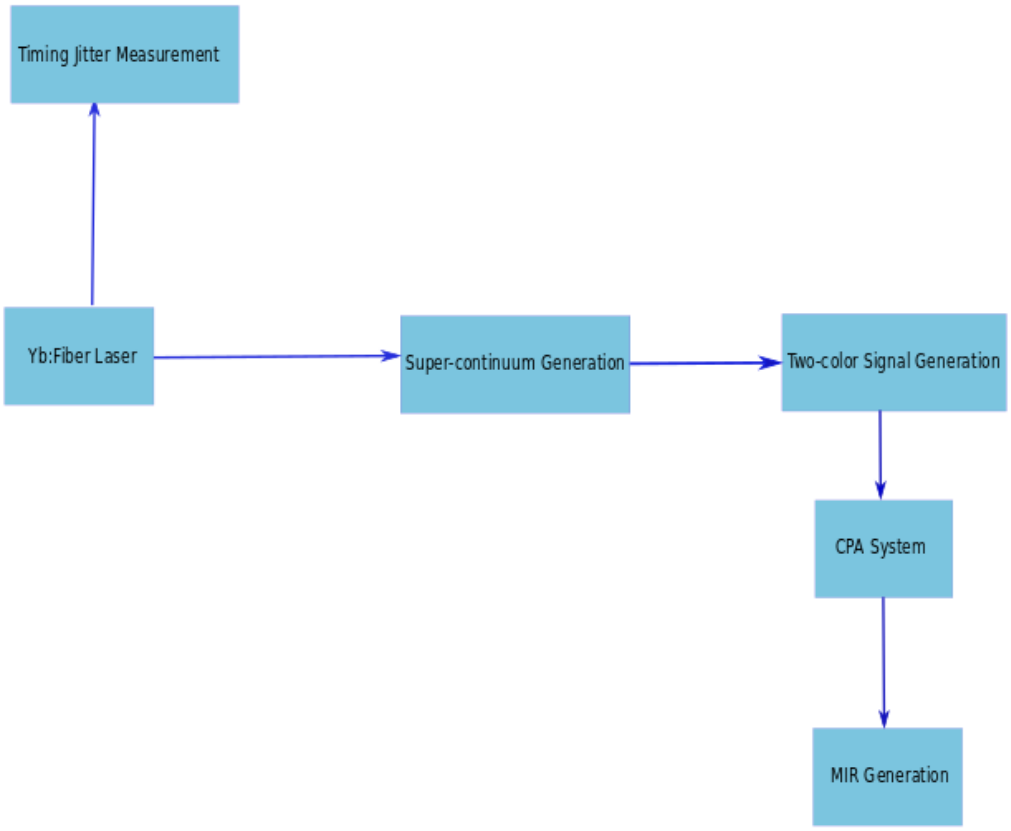

Figure 3.1: Sketch of the entire experimental setup

3.1 Two-color Yb:fiber CPA System

3.1.1 Super-continuum Generation

The laser source used as the front end of our two-color amplification system is a Yb:fiber femtosecond laser containing an oscillator and a CPA system in a compact commercial package. The Yb:fiber laser generates pulses with the width of around 200 fs at a repetition rate of 65 MHz. In this mode-locked laser, a rare-earth doped fiber, Yb, is used as high gain medium in the oscillator and the amplifier. For such a high-gain, fiber-based laser, mode-locking instability or fiber-end damage can be caused by a small μW level noise from the reverse-direction light. Such is a disadvantage of mode-locked, rare-earth, doped-fiber lasers compared to mode-locked, solid state lasers [50]. As shown in Figure 3.3, output pulses passed through a Faraday isolator in order to protect the laser source from the radiation reflected by the CFBG. This isolator contains three main components: an input polarizer or birefringent crystal, a Faraday rotator and an output polarizer. This combination allows

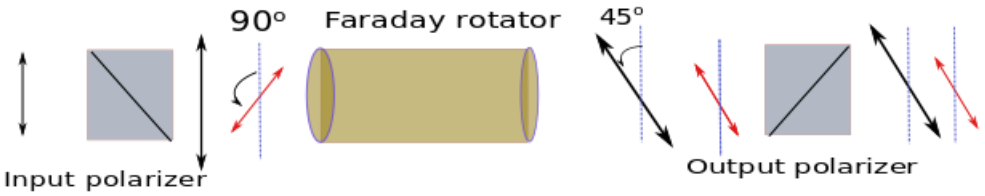

Figure 3.2: Schematic illustration of a Faraday isolator: *the forward light polarization (black lines) is rotated by* 45^0 *after the Faraday rotator. The output polarizer is aligned at* 45^0 *with respect to the input polarizer to let the light pass through. The backward light (red lines) passes through the output polarizer and then its polarization is rotated by another* 45^0 *after the Faraday rotator so its polarization is different from that of the input light by* 90^0.

light to travel through the isolator only in the forward direction by rotating the incident light's polarization plane by 45^0 while maintaining the light to be linearly polarized. This is illustrated by Figure 3.2. The Faraday isolator used in this setup had 60% transmission. The pulses, then, propagated through a half wave plate (HWP) before they were coupled into a AND PCF via a 20× microscope objective lens to generate a SC. That PCF is 2 m long. The spectrum content of the SC could change by rotating the HWP in front of the PCF to change the polarization of the incident pulses. This helps with choosing a desired ratio between the two colors in the input signal of both the pre-amplifier and the MIR generation.

3.1.2 Two-color Signal Generation

Previously, a two-color signal had been selected from a SC by using interference or notch filters [16, 51]. The required number of interference filters depends on the expecting separation between the two colors in the output signal. One advantage of using notch filters is its flexibility in selecting the spectral wavelength. However, using them also has some disadvantages. Firstly, their rejection bandwidth is limited, as short as around 45 nm, so in order to make a 60 nm separation two identical filters in series should be used. This, as a result, causes a high power loss.

In our case, an improvement was made by using a CFBG. This CFBG was spliced to the PCF and the 100 m fiber stretcher, as seen from Figure 3.3. The output spectrum was a two-color signal spectrum with a sharp and clear spectral ejection with a 60 nm bandwidth, from 1025 nm to 1085 nm, centered at 1055 nm.

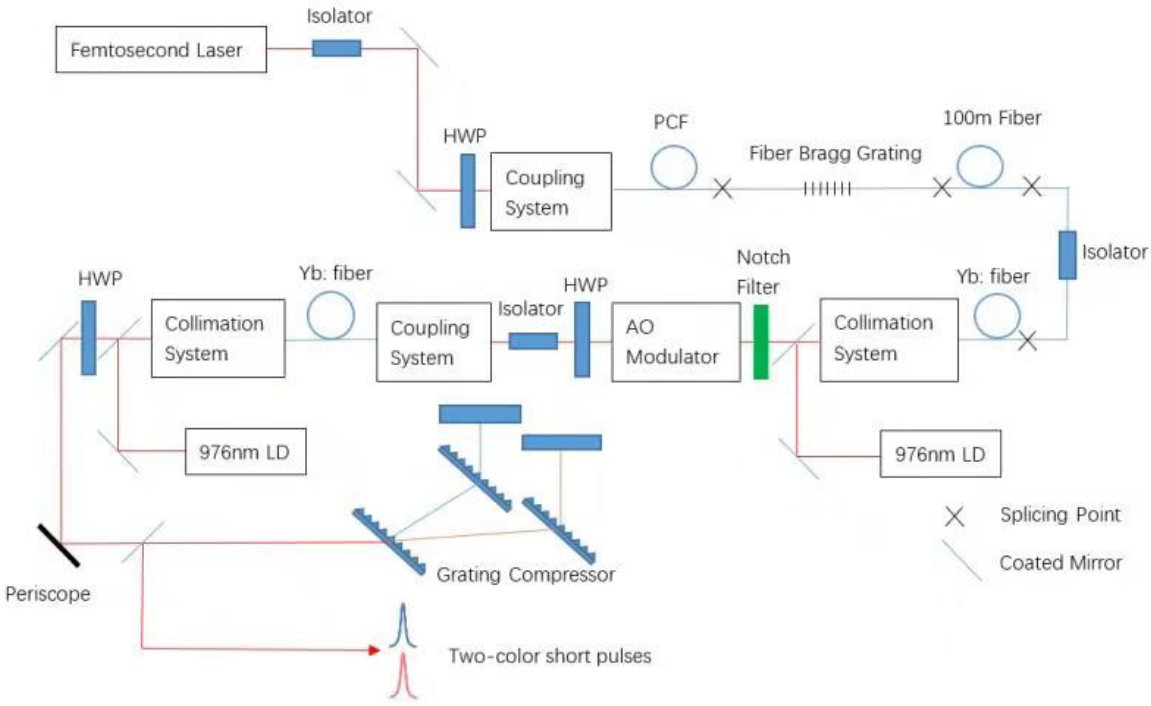

Figure 3.3: Experimental setup up to the CPA system

3.1.3 Two-color Yb:fiber Pre-amplifier

Figure 3.3 shows the full setup of this stage. After being stretched by the 100 m fiber, the peak power of the pulse was dramatically decreased so it could be safely amplified in the next stages. The 1025 and 1085 nm pulses were stretched by an amount of 16 and 13.5 ps, respectively. The output pulses continued to propagate into an Yb:fiber to be amplified after passing through a fiber-embedded Faraday isolator. The reason for this isolator's presence was to avoid the ASE sent back from the Yb:fiber pre-amplifier to the previous parts of the experimental system.

In the two-color pre-amplification stage, a single mode and double clad Yb:fiber with a length of around 1.8 m and a core diameter of 8.6 μm was employed. This Yb:fiber has a gain peak at approximately 1035 nm. Especially, in this stage, it is worth to mention that one end of this Yb:fiber and the 100 m fiber stretcher were spliced together through the fiber-attached Faraday isolator to increase, first, the seed-to-fiber coupling efficiency and second, the stability of the system. This can be considered as an important improvement in the amplification process. Therefore, counter-pumping was still applied in the pre-amplifier. In fact, experimentally, we found that there was no dramatic difference in the pre-amplification output between co-pump and counter-pump. The pump, a diode-laser

that is coupled to a multi-mode fiber, can generate a power of 6.5 W for the pre-amplifier. In addition, as it has been shown that the emission cross section of an Yb:fiber can be maximized, at around 1035 nm, by pumping at 975 nm. In addition, the absorption bandwidth of the Yb:fiber is narrow and the diode-laser pump's output wavelength depends on the diode's temperature. Thus the diode-laser pump's temperature of this stage was controlled to have the pump's spectral peak at 975 nm as desired. Besides, the two long-pass dichroic mirrors were placed right after the diode pump to protect the pump from the amplified signal that can travel backward because such dichroic mirrors reflect the pump beam while transmit the amplified seed. These two mirrors are optimized for 90^0 reflection. One short-pass dichroic mirror was also put at the output of the pre-amplifier to let only the amplified signal be reflected to the next stage. Note that, dichroic mirrors are sensitive to light polarization and wavelength. Therefore, this short-pass dichroic mirror's angle was carefully and finely tuned to optimize the output power.

3.1.4 Two-color Yb:fiber Main Amplifier

Before being amplified in the main amplifier, the pre-amplified output signal was sent to a notch filter, next, a HWP and then a Faraday isolator (Figure 3.3). The transmission of this isolator is roughly 50%. Finally, the two-color-without-ASE signal was coupled into an Yb:fiber which is counter-pumped by a diode laser pump.

First of all, it was necessary for a notch filter to be placed after the pre-amplifier because there was some ASE in the two-color signal after that stage. Secondly, it is obvious that the Faraday isolator helped block the ASE from the main amplifier to travel back to the previous amplification stage. Especially, the first difference in the setup between the two stages was that, in this amplification stage, the Yb:fiber did maintain the polarization of the signal while that of the pre-amplifier did not. As the two colors were still linearly polarized but they might have different polarizations. Hence, the HWP played a very important role in changing the power ratio between the two colors by changing their polarization planes. This was crucial to MIR optimization. The fiber core has a diameter of 11 μm. The second difference was that the input signal was free-space coupled into the Yb:fiber main amplifier. Therefore, the pre-amplifier was better in terms of stability and coupling efficiency. Finally, one more long-pass dichroic mirror was placed right after the Faraday isolator to avoid the strong ASE from the pump traveling back to the Yb:fiber in the previous stage. Other than that, the two stages had common characteristics, in particular, the diode laser pumps peaked at 975 nm were both controlled in temperature for the reason mentioned in the pre-amplifier setup. In addition, the pump powers were around 6.5 W and two long-pass dichroic mirrors were also used to protect the diode laser pump. The short-pass dichroic

mirror at the output end of the stage was rotated to optimize not only the output power but also the spectrum. We found that this mirror could significantly block either the short or long wavelength side of the amplified spectrum. So it is paramount to find a proper angle for the mirror to have an expected output. In our case, the angle was around 45^0.

3.1.5 Pulse Compression

The goal of the compression, as it is called, was to compress the pulse back to its original pulse-width, ideally, when it had been already amplified. In our experiment, a Treacy grating compressor [31] was used. This was a set of three identical gratings. Particularly, they all were transmission gratings with the same groove density, 1250 lines/mm, and the same Littrow angle, 41.7 degrees at 1064 nm. In addition, their operating polarization is TE (s-polarization).

There are a few main requirements for the compression setup. Firstly, the three gratings have to be set to be parallel to each other. This can ensure that the pulses are not spatially chirped. Practically, we sent the compressed beams to the spectrometer and tweaked the horizontal knob of the mirror in front of the spectrometer to make sure that the beam spectrum did not shift horizontally. Secondly, the light's incident angle should be at or close to Littrow angle to minimize the power loss from each grating. The third requirement is about the signal's polarization. As the grating's operation is optimized for s-polarized signals, thus, it is important for the incident light to be s-polarized. Finally, the distances between each color's grating and the first grating, namely compressor length is the key point in the compressor. In practice, for each color, the background-free autocorrelator was used to compress the pulse.

The pre-step for the compressor in our experiment was to convert the signal's polarization from p-polarization after the main amplifier to s-polarization by a 90^0 periscope. The output signal from the main amplifier hit the bottom mirror of the periscope and then was reflected straight up to the top mirror which caused the reflected beam's direction to change by 90^o with respect to the incident beam of the periscope, and thus, to change the polarization of the beam by 90^0.

The compressor is described in Fig 3.3. First of all, the two-color signal was diffracted from the first grating and each color, then, separately traveled to its own grating. The back mirrors after each color's grating sent the two colors back to the first grating. In this setup, all the gratings were aligned in such a way that the incident beams were vertically above the reflected beams. Furthermore, when the two colors traveled back to the first grating, the 1085 nm color was below the 1025 nm color. Besides, as for the MIR generation purpose, the two compressed colors later need to be temporally collapsed or synchronized.

Thus, the 1025 nm back mirror was placed on a translation stage for fine movement.

3.2 Ultrafast MIR Generation

The nonlinear crystal used to generate MIR at 18.5 μm by DFG is GaSe that is 1 mm thick. In order to make the DFG happen in GaSe, the two colors need to overlap both temporally and spatially. The former can be carried out by moving the back mirror on the translation stage of the compressor. The latter can be performed by using a polarizing beam splitter (PBS) as shown in Figure 3.4. This optical device is commercially designed to reflect the s-polarized beam while transmit the p-polarized one. Therefore, another 90^0 periscope was placed in front of the PBS to flip the polarization of the 1085 nm color to p-polarization. On the other hand, it is noticeable that the 1025 nm color's polarization was kept to be s-polarized after the grating compressor. However, it is because the DFG is optimum in the crystal GaSe if the red and blue color are s-polarized and p-polarized, respectively [52]. As a result, there was another periscope used to one more time rotate or 'swap' the polarization of the two colors simultaneously before they both enter the crystal. Next, the two beams were focused on a GaSe crystal by different converging lenses with various focal lengths such as 100 cm, 40 cm, 30 cm and 25 cm. For each lens, two different setup schemes were used to optimize the MIR detection on the MCT and on the thermal detector Gentec XLP12. The reason why different lenses vs. different detection schemes were used to optimize the unexpectedly low MIR power. It is because in a previous work done by a co-worker [16] [22], the MIR power was stated to be at mili-Watt level due to the misunderstanding in the detectivity of the MCT detector. We found out that the actual power was at micro-Watt level by measuring the MIR by a thermal detector for confirmation.

The first detection-setup scheme was similar to [16], i.e, a spherical converging mirror of which the focal length is 5 cm was placed after the GaSe crystal and on the propagation path of the generated MIR. This mirror was placed on a translation stage to optimize the detected MIR. The reflected light from the spherical mirror was then focused perpendicularly on the MCT by a flat gold mirror. As spherical mirrors have been said to cause aberration if the angle between the incident and reflected light is non-zero. Therefore, the spherical and flat mirrors should be aligned in such a way that the angle can be as small as possible. To preclude the aberration, the flat mirror should be placed close to the spherical mirror as much as possible. In fact, the question "How far away from the GaSe crystal should the spherical mirror be placed?" should be investigated carefully for two main reasons. The first reason is to collect the generated MIR after the crystal as much as possible on a spherical mirror of 2.5 cm in diameter. Because at a distance z away from

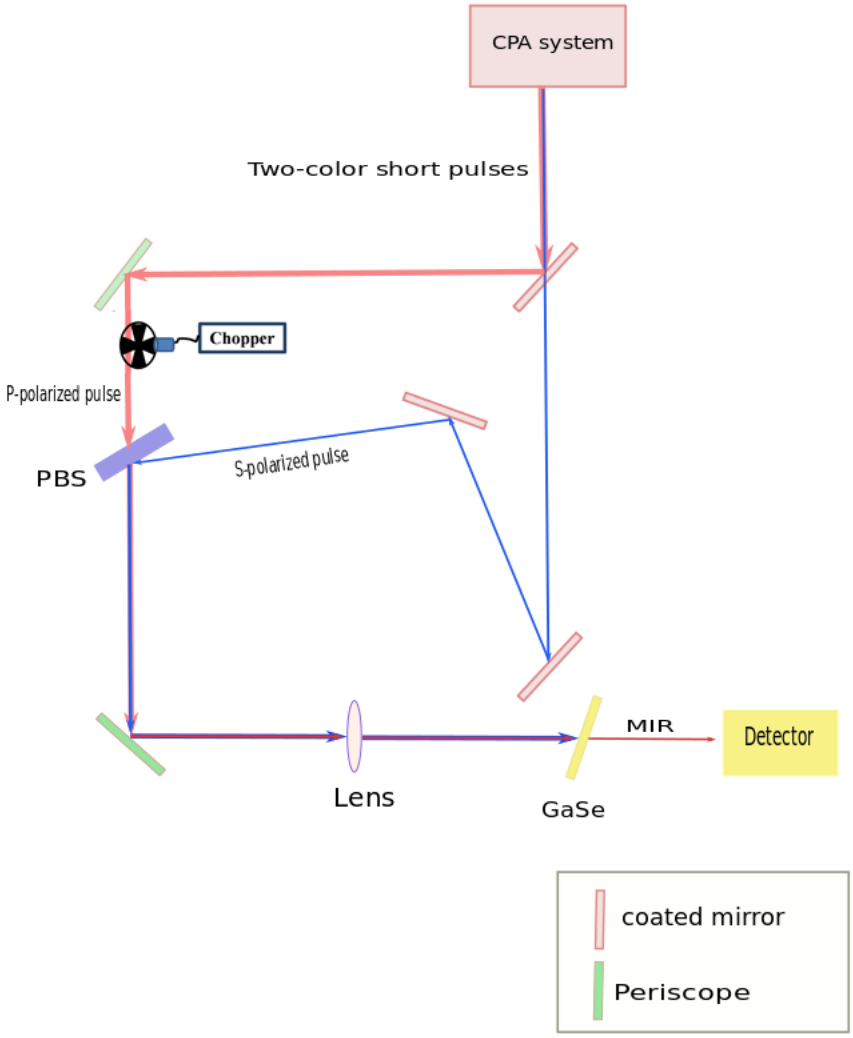

Figure 3.4: Setup for MIR generation

the crystal, the beam diameter of the 18.5 μm wavelength is 18 times bigger than that of the IR signal and pump and may exceed the mirror diameter. The radius of the focused beams on the crystal can be found by using the following equations:

$$w_0 = \frac{2f\lambda}{D\pi} \tag{58}$$

where f, λ, D are focal length, wavelength and beam diameter at the lens. So, the MIR beam radius at a distance z away from the crystal is calculated by

$$w\left(z\right) = \frac{w_0}{\sqrt{2}}\sqrt{1 + \frac{z^2\lambda^2}{\pi^2 w_0^4}} \tag{59}$$

The second reason is optimize the MIR detected on the detectors. In the case of detecting the MIR by the MCT, the active window size is small, 1 mm, so the focused spot on the MCT should not exceed this number. However, when measuring the MIR by the thermal detector, for the power meter's safety, it could not be put right at the focal point of the spherical mirror. Instead, it was placed further away where the MIR beam spot started diverged quickly as the smaller the focused spot was, the faster the spot size diverged after that focused position. In addition, the active aperture of this device is also finite, 12 mm, which could block some incoming MIR. Therefore, both of the lens's focal length and the spherical mirror position needed to be considered simultaneously in each measurement to optimize, first, the MIR generation in the crystal, and second, MIR detection. In this scheme, for the goal of making a magnification of 1 for the MIR beam on the MCT, the spherical mirror was at 10 cm away from the crystal and distance from the spherical mirror to the MCT was also 10 cm, then the MIR was optimized on the MCT. The setup is shown by Figure 3.5.

In the second setup scheme for MIR detection, an off-axis parabolic mirror with a focal length of 5 cm was used to replace the spherical mirror. In contrast to spherical mirrors, off-axis parabolic mirrors could do a better job than the spherical ones in terms of avoiding the spherical aberration. The experimental sketch is shown in Figure 3.6. A flat gold mirror was placed very close to the crystal to collect as much of the MIR as possible. Then, the light was reflected to the off-axis parabolic mirror which was placed on a translation stage. Finally, the MIR was focused on the MCT. The distance from the crystal to the off-axis parabolic mirror was approximately 7 cm. Again, this was found by practically optimizing the MIR on the MCT.

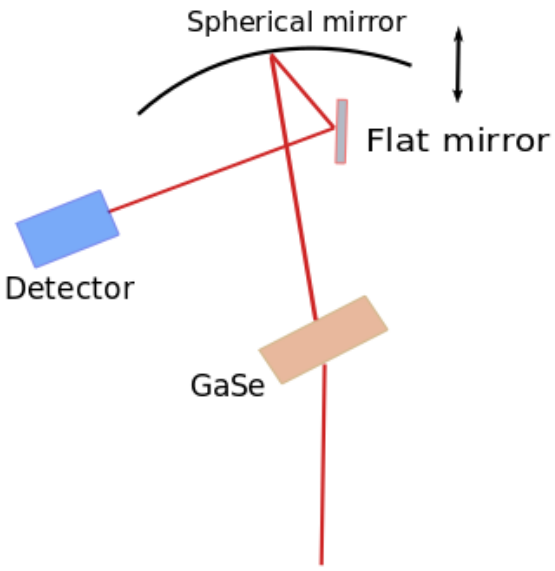

Figure 3.5: Illustration of the first scheme setup

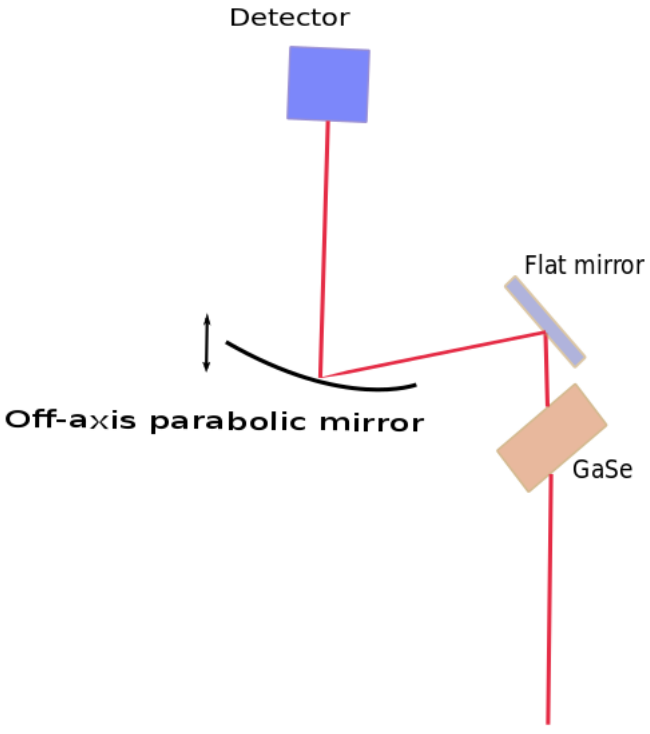

Figure 3.6: Illustration of the second scheme setup

In both schemes of detection, the MCT was always used first in order to optimize the alignment because this sensitive and fast-response photoconductive detector is able to spot a relatively weak MIR signal.The MCT was cooled by liquid nitrogen since, theoretically, the longer the wavelength was the lower temperature the detecting material should have. The full set of the detection composed of a mechanical light chopper, a lock-in amplifier and the MCT detector. The lock-in amplifier can be considered as a phase sensitive detector. It means that it measures the AC signal that has the same frequency and phase as the reference signal. The AC signal and the reference signal mentioned above were created by the chopper rotation. The chopper wheel was set to rotate at a constant frequency, nearly 1 KHz in our case, to chop the red color. This not only interrupts the signal path to make the signal from the detector become AC but provided the reference signal for the lock-in amplifier as well. As a result, only the AC signal that was coherent with this reference waveform or the MIR could be measured, while the noises were rejected. Besides, a 1mm-thick Germanium (Ge) filter was placed in front of the MCT's detecting window to block the IR signals that transmitted through GaSe and to allow only MIR passing through. The transmission of the Ge filter for our 18.5 μm was around 35%.

Technically, the MIR could be enhanced by finding the right phase matching angle, azimuthal angle, proper ratio between the two incident colors, temporal and spatial overlap, and spatial walk-off angle between the pump and signal. Practically, the phase matching and azimuthal angles were found by rotating the nonlinear crystal, GaSe, around its vertical axis and optical axis, respectively. The phase matching angles theoretically found in our case were 12.06^0 for type I and 12.45^0 for type II by using equations (50)-(52). The HWPs helped with the ratio between the blue and red color. Finally, their temporal overlaps could be improved by using the translation stage in the compressor. The walk-off angles calculated for the wavelength of 1025 nm were around 3.48^0 for type I phase matching and 3.6^0 for type II phase matching. One possible method that was applied to test whether the two colors were together temporally and spatially by optimizing their resultant sum frequency generation after a second harmonic generation crystal, specifically β-barium borate (BBO) was used in our case.

3.3 Timing Jitter Measurement

The main idea was comparing the autocorrelation width of the same pulse and adjacent pulses. The autocorrelation widths were measured by employing the background-free intensity autocorrelator (non-collinear autocorrelator). The timing jitter measurement was performed right at the output end of the laser source. For precision, the light beam was collimated by a telescope before they enter the same autocorrelator so that the beams from

the two autocorrelation arms always had the same size all the way to the SHG crystal. In addition, in order to ensure of high stability and good alignment, and hence, precise measurement of the autocorrelator, a Michelson interferometry was used for the case of the same pulse. This interferometry, in fact is the collinear autocorrelation. It means that when interference occurs, the ratio between the peak of the interference and background should be 8:1. This step is a test if the alignment was good.

Figure 3.7 shows full setup of the autocorrelator. The light beam passed a telescope containing a pair of two convex lenses ($f_1,\ f_2$) of which the distance is equal to $f_1 + f_2$. Practically, the telescope (25, 10) cm was used to collimate the beam from the Yb:fiber laser. Then, the collimated beam was split by a beam splitter which was aligned around 45^0 with respect to its incident beam. As a result, one beam transmitted through the beam splitter and one was reflected by an angle of 90^0 by the splitter. Next, the beam on each arm was reflected straight back after hitting two mirrors perpendicular to each other. The reason why a pair of 90^0 mirrors was used instead of a single mirror was to prevent the backward lights from going back to main amplification fiber. However, the experiment was required to be background free or non-collinear which means that one arm beam had to be raised to be vertically higher than the other. When the reflected beams from two arms were recombined at the splitter, they were focused on the crystal BBO by a 10 cm focal length convex lens. This setup was applied in both cases of same pulse and adjacent pulse non-collinear autocorrelation. Nevertheless, the only difference or change was that in the former case, the optical path length that lights traveled in two arms must be the equal, whereas, the latter required the difference in the optical path length to be

$$\Delta L = \frac{1}{2} cT \tag{60}$$

where c=3.10^8 m/s was used as the speed of light in air, $T = \frac{1}{f_{rep}}$ (s) is the period of the laser pulses. The appearance of the coefficient $\frac{1}{2}$ in equation (60) is due to the fact that the light traveled a round trip on each arms. In our case, $\Delta L \approx 2.3$ m. In addition, in order to achieve the width of the autocorrelation pulse, the back mirrors of one arm, we chose the short arm's mirrors, were placed on a translation stage which was driven by a motor controller with the resolution up to 0.1 μm.

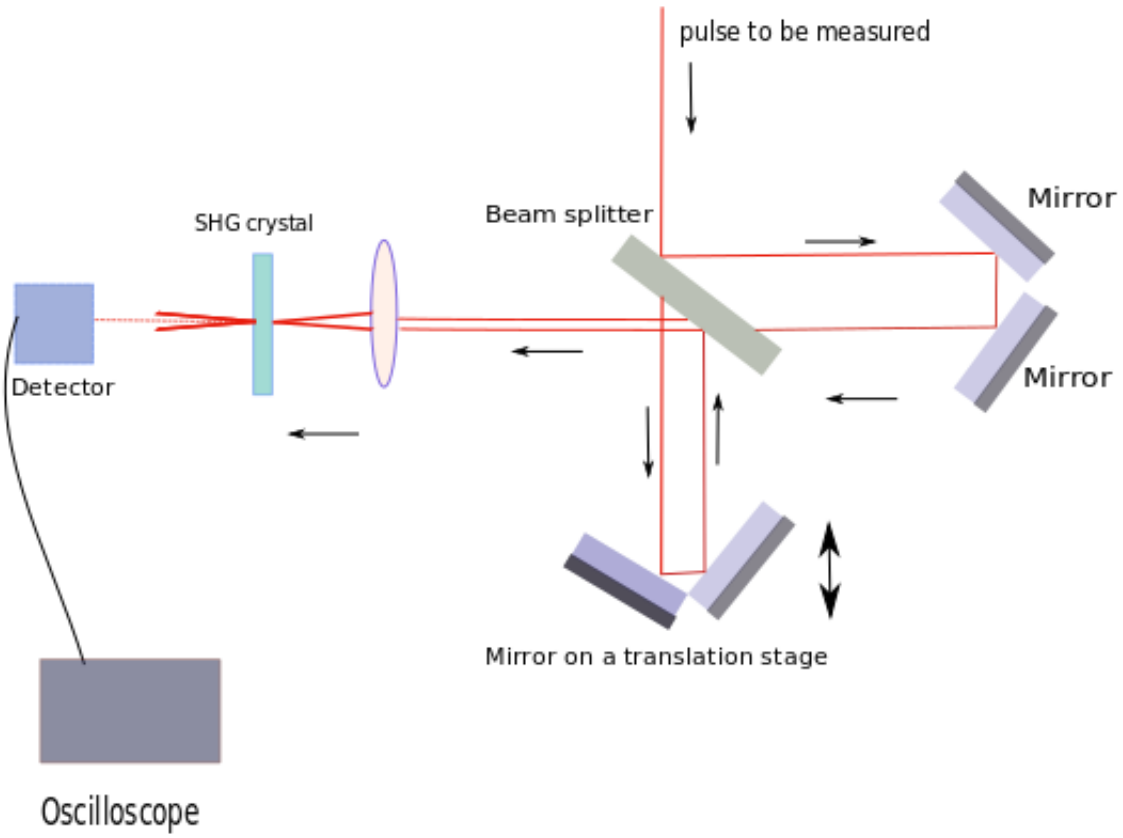

Figure 3.7: Cross correlation setup

4 Experimental Results and Discussion

4.1 Super-continuum and Two-Color Signal Generation

A 200 fs seed pulse was generated by a 65 MHz Yb:fiber laser source. It could produce an average power of around 0.5 W as well as a spectral FWHM bandwidth of 5 nm. The peak of the spectral bandwidth was around 1040 nm as shown in Figure 4.1.

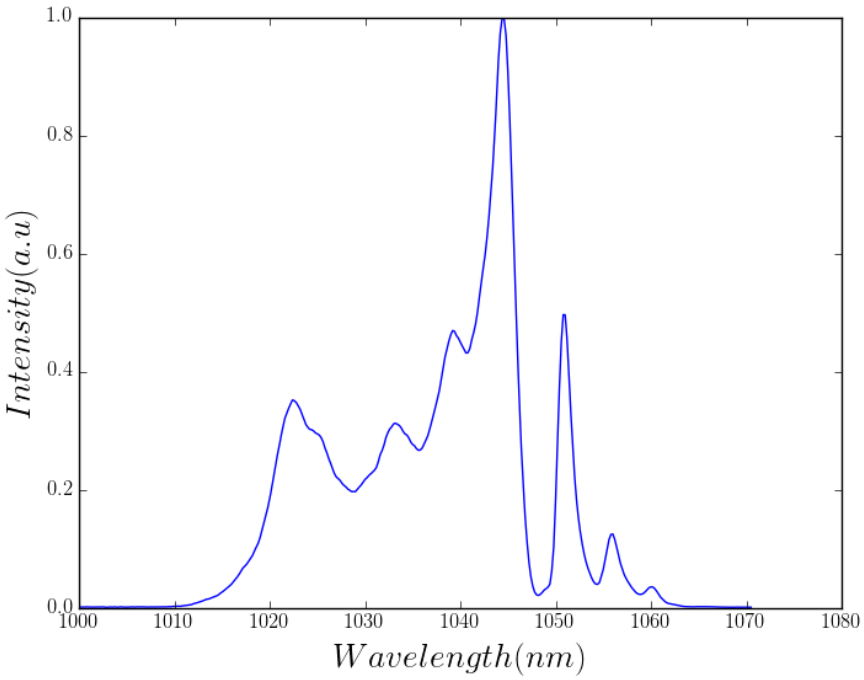

Figure 4.1: Spectrum of Yb:fiber laser

The coupling efficiency into the PCF was estimated to be approximately 35%. The SC spectrum after the PCF had a fixed peak at around 1035 nm and a range of average power measured from 90-100 mW depending on the HWP's angle in front of the PCF. Moreover, the angles could determine the power ratio of the two-color seed for the amplification stages. Figure 4.2-4.4 shows different cases of the 1025 v.s 1085 nm power ratio under the same scale with respect to an angle of $70^0, 180^0, 200^0$ of the HWP. The blue and green circles on the spectra show the power of the 1025 and 1085 nm, respectively to help visualize how the HWP impacted the ratio between them.

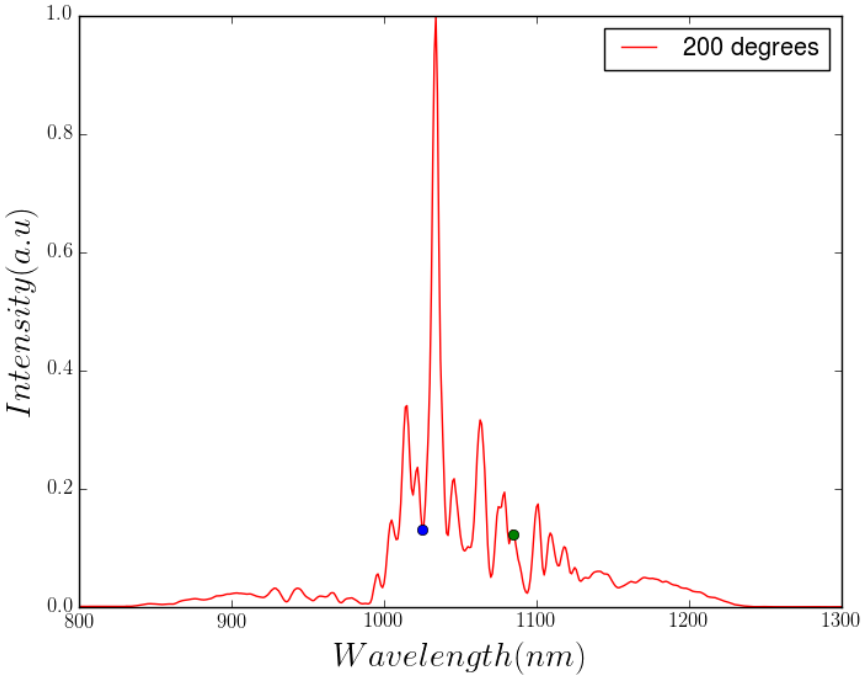

Figure 4.2: Super-continuum after the PCF at an angle of 200^0 of the HWP

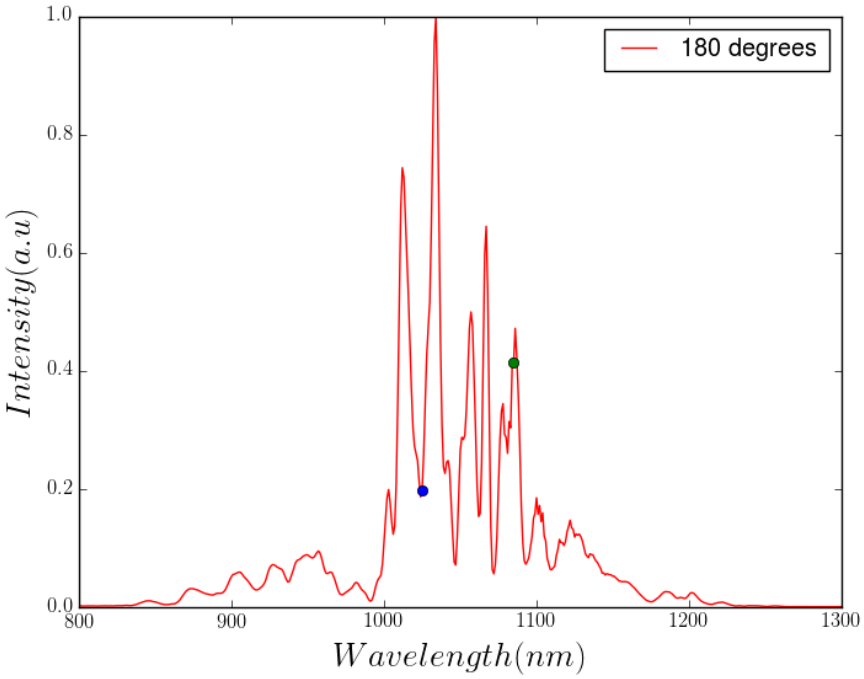

Figure 4.3: Super-continuum after the PCF at an angle of 180^0 of the HWP

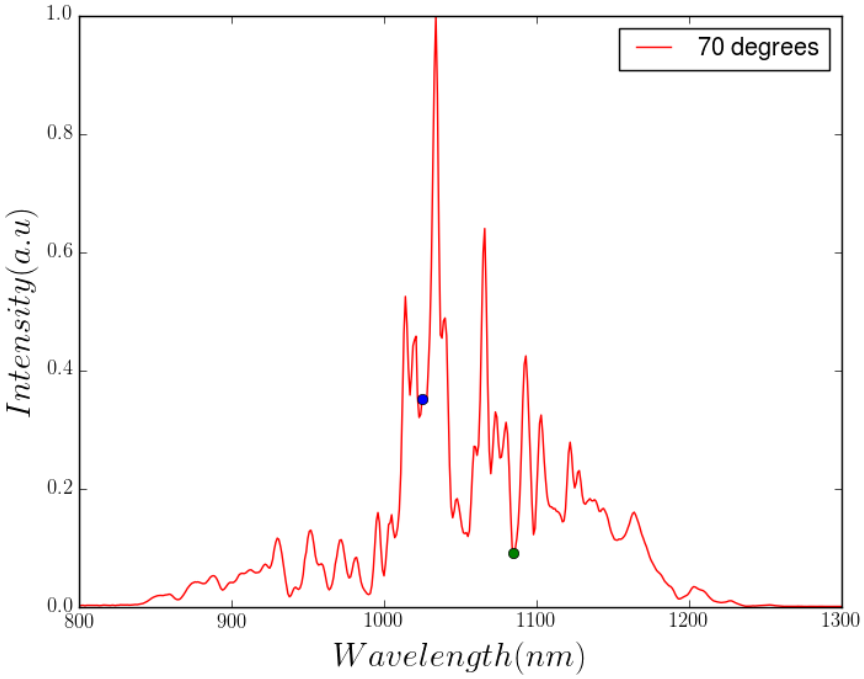

Figure 4.4: Super-continuum after the PCF at an angle of 70^0 of the HWP

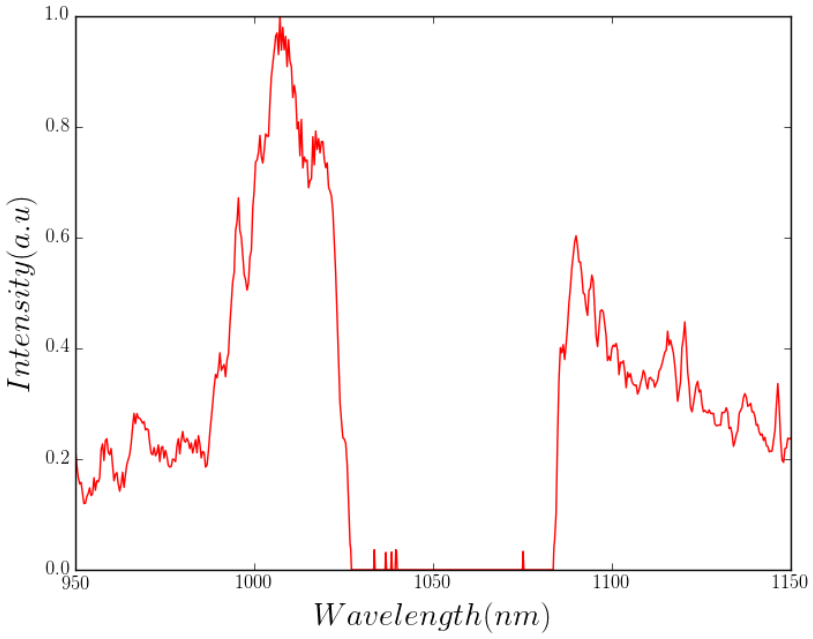

Figure 4.5: Input spectrum of pre-amplifier

After propagating through the CFBG, a bandwidth of 60 nm, starting from 1025 nm to

1085 nm, was clearly cut off from the SC. The spectral input of the pre-amplifier is shown in Figure 4.5. An average power of 25 mW on average was the pre-amplification input.

4.2 Two-Color Yb:fiber CPA System

The seed of the two-color Yb:fiber CPA system is shown in Figure 4.5. The total power as well as the power ratio between the two colors could be varied by the HWP placed in front of the PCF. As the peak gain of the Yb:fibers used in the two amplifiers was approximately 1035 nm that was closer to the two wavelengths, 1025 nm and 1085 nm, so these two wavelengths were dominantly amplified more than the two outer-edge wavelengths of the spectra. Thus, the amplified spectra experienced a gain narrowing effect.

In the pre-amplification stage, the coupling efficiency was approximated to be almost 40%. As a result, the seed at a power of a few tens of mW level (less than 30 mW), was amplified to almost 870 mW. The full output spectrum shown in Figure 4.6 reveals the presence of a small portion of ASE between the two colors. After the ASE had been removed by an interference filter, not only the power but also a portion of the spectral width on the short-color side reduced dramatically as seen in Figure 4.6. It is because of the sharpness of the edge of the filter. Specifically, the pre-amplified signal power decreased by almost 50% from 865 mW before the notch filter to 450 mW after the notch filter.

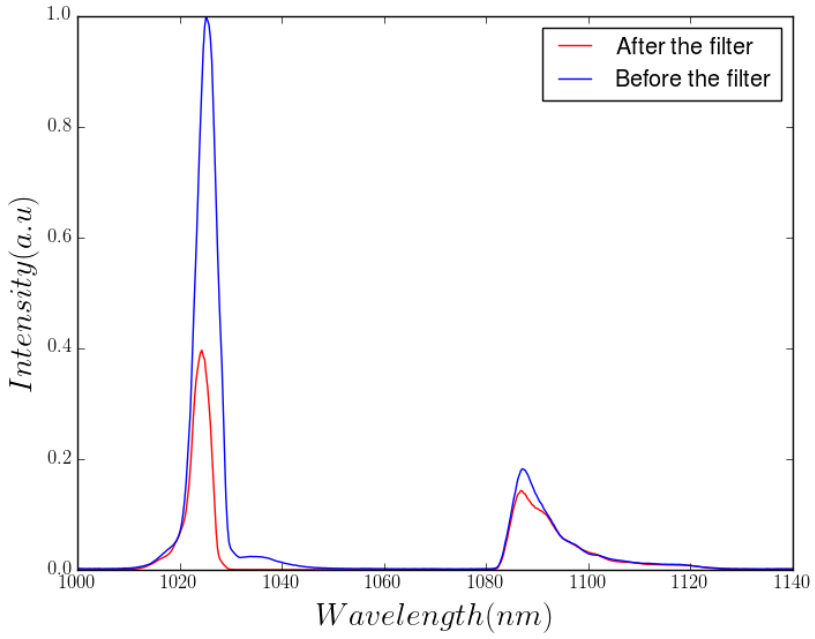

Figure 4.6: Output spectrum of the pre-amplifier before and after the notch filter

This power kept decreasing one more time by ∼40% after traveling through another Faraday isolator before entering the main amplification Yb:fiber. This is equivalent to a power drop to $150 - 250$ mW. The reason why there was a wide range of power after the isolator was because of the HWP set in front up the isolator. This optical device did play an important role in rotating the polarization plane of the signal to match that with the polarization of the isolator and, thus, of the Yb:fiber of the second amplification stage. Correspondingly, the output power range after the main amplifier was around 3.4-3.5 W. It is clearly seen that although the input of the main amplifier had a wide variation range, its output power almost stayed around the same value as shown in Figure 4.7 and 4.8. In fact, the input power did have a significant impact on the ratio between the two colors of the output but the total power. Particularly, in two cases of the HWP's angle differing by 45^0, at 124^0 (Figure 4.7) and 170^0 (Figure 4.8), the total input power of the main amplifier mostly was determined by the power of the long color. However, the power of the 1085 nm color in this stage was proportional to its input, in other words, the more power in 1085 nm color the input had, the more power in that color the output could produce. This is one advantage of our experimental system because it helps with determining the desired short:long ratio for the MIR generation. Moreover, as is shown by Figure 4.7 and Figure 4.8, after the main amplifier, the FWHM bandwidth of both colors were greatly reduced to nearly 4.5 mm and 7 nm for the 1025 and 1085 nm color, respectively.

Once the signal had been amplified, it was compressed to maximize its peak power. Ideally, the incident angle of the incoming signal to the gratings in the compressor should be at Littrow angle, 41^0 to minimize the power loss. Nevertheless, the three gratings were aligned to be parallel to each other but the signal consists of two wavelengths differing by 60 nm. So, finally, they entered their own gratings at different angles after being diffracted from the first grating. Therefore, the angular orientation here turned out to help one of the color signals only. Our choice was optimizing the short color so the incident angle to the compressor was to support the 1025 nm color. Experimentally the compressor length were found to be approximately 57 mm and 98 mm for the short and the long wavelength, respectively. After the compressor, the long and short suffered a loss of approximately 50% and 30%, respectively. This is equivalent to an average power of 0.7 W and 1.4 W for the case indicated in the bottom graph of Figure 4.7, leaving a total average power of 2.1 W of the two colors. Furthermore, the resultant compressed pulse-widths of the blue and red color measured by an intensity autocorrelator were 900 and slightly under 600 fs, respectively. Last but not least, the system alignment stability was highly improved compared to [16, 22], i.e., our system can be stable up to 30 minutes.

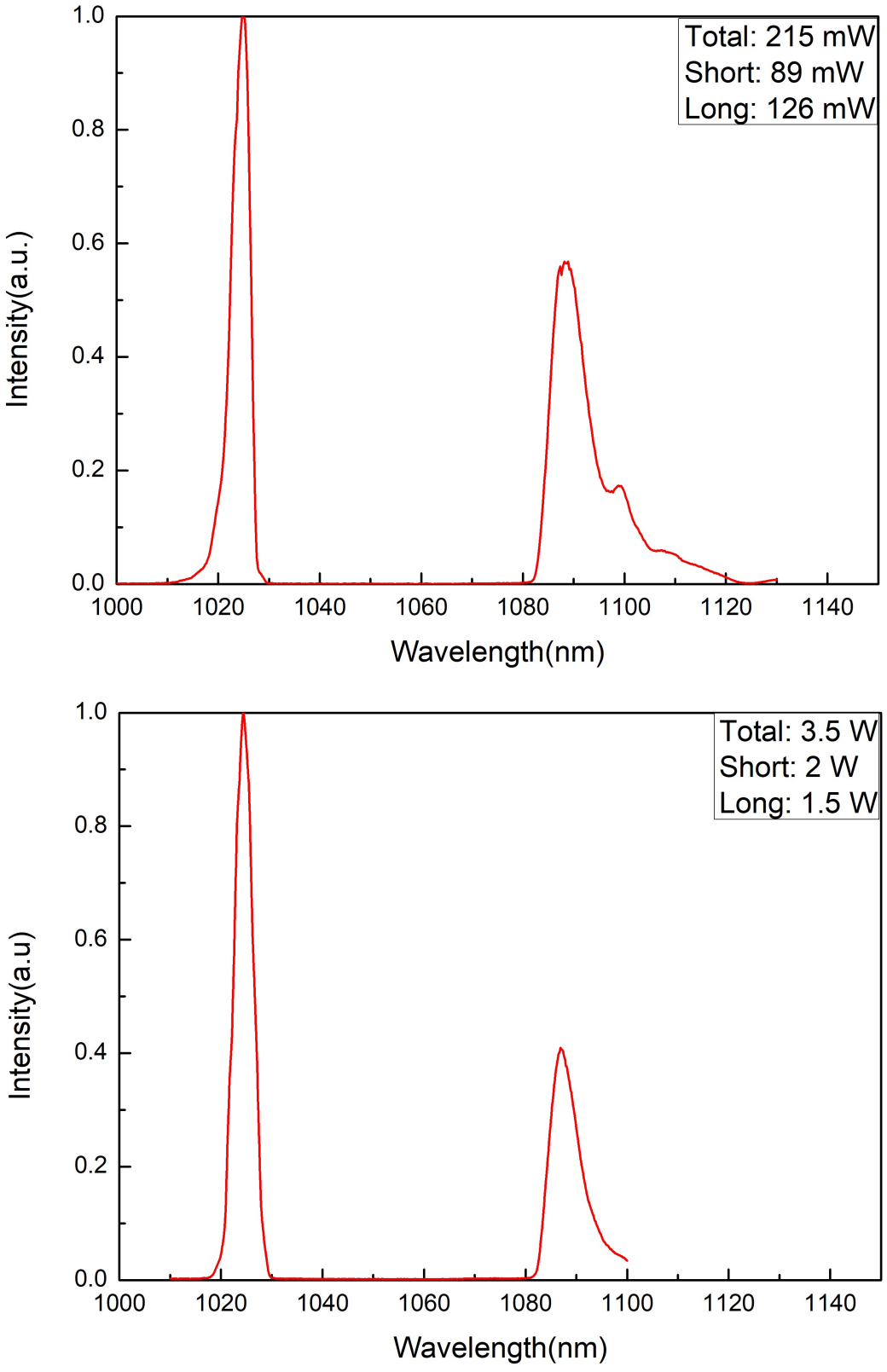

Figure 4.7: The input (top) and corresponding output (bottom) spectra of the main amplifier when the HWP was at 124^0

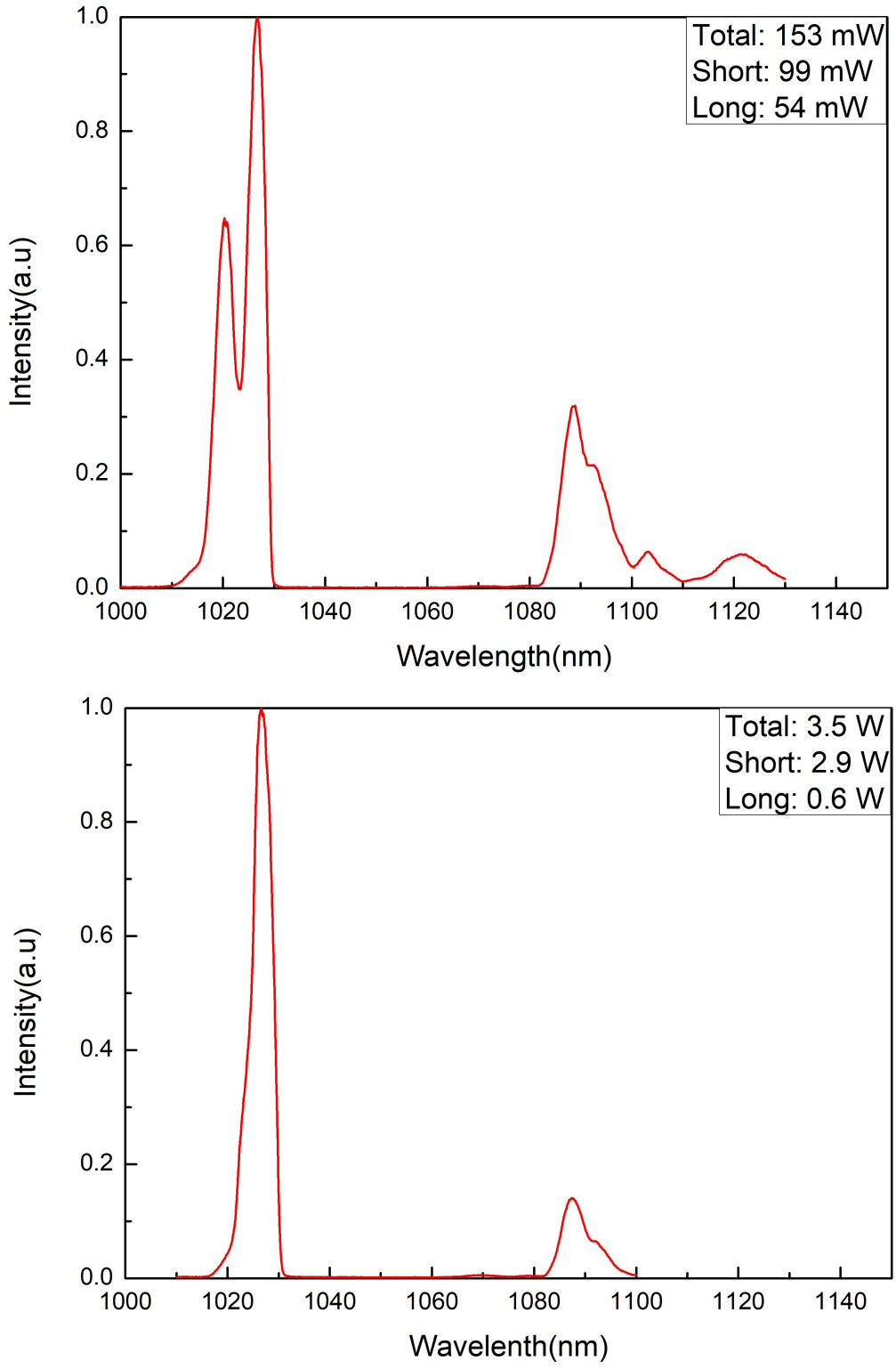

Figure 4.8: The input (top) and corresponding output (bottom) spectra of the main amplifier when the HWP was at 170^0

4.3 Ultrafast Generated MIR: Results and Discussion

Overall, after using lenses with different focal lengths together with the two setup schemes for MIR detection described in section 3.2, we found that the 25 cm focal length lens gave optimum MIR on both MCT and thermal detector. In addition, for each lens, the detected MIR on the MCT and the thermal detector was always higher when using the spherical mirror setup compared to the setup that used the off-axis parabolic mirror. For the lens of 25 cm focal length, the optimum MIR detected on the MCT was 1.4 V, shown on the lock-in amplifier. On the thermal detector, it showed a MIR average power in the range of 150-180 μW. This already took the 35% transmission of the Ge filter into account.

Our results confirm that with an input of a few-Watt-level average power and sub-picosecond pulse-width, the DFG method can produce a few-hundred-microWatt-level average power of MIR at 18.5 μm. MIR at 18.5 μm was already generated in our previous work [16] in which the MIR is tunable from 16 μm to 20 μm. However, in our current system, the total average input power of the pump and signal is 40 % higher in comparison. Additionally, we achieved better pump:signal power ratio, 2:1, to maximize the intensity product between them, $I_p I_s$ as stated in equation (49). According to this equation, the MIR average power can be rewritten in terms of average power P_p, P_s, pulse width τ and beam areas A as

$$P_{MIR} \sim \frac{P_P P_s L^2}{A \tau f_{rep}} \tag{61}$$

where $I = \frac{P}{\tau f_{rep}}$. In this equation, all the beams were assumed to have the same area A and same pulse width τ which is not true in reality.

Theoretically, the MIR intensity can be optimized if the pulses are compressed well. However, in this project, the compressed blue-color pulse-width that we currently achieved is almost 50% longer than that in [16]. Especially, both of the compressed colors' pulse-width are 3 times, for the long, and nearly 5 times, for the short, longer than the laser's initial pulse-width. There are three main reasons for the issue of obtaining the initial transform-limited pulse-width. The first reason is gain narrowing effect. This effect occurs in both of the amplification Yb:fibers because of their finite gain bandwidth. It means that on the two color spectrum, the wavelengths which are closer to the gain peak are amplified more dramatically than the rest. Figure 4.9 shows the ASE spectrum of the main Yb:fiber amplifier when there is no seed. As can be seen from the graph, when an Yb:fiber is pumped at 975 nm, the gain peak is approximately 1035 nm. This means that the short encounters more gain narrowing than the long as it is closer to the gain peak of Yb:fibers. In consequence, the short color always has longer pulse width than the long

color and more importantly they cannot be compressed to their initial pulse-width. High-order-dispersion can be the second reason. In a CPA system, ideally, SOD and TOD in the stretcher and all the amplification media or materials should be compensated by those in the compressor. It was shown by the author of [26] that grating compressors can cancel the SOD and TOD of grating stretchers but other optical media including fibers. This reveals that in our system the TOD existing in the 100 m fiber stretcher and Yb:fiber amplifiers may not be compensated. However, according to our calculation in [48], the TOD itself produced in our home-built CPA system can not be in charge of this whole issue. Besides, the pulses coming out of the Yb:fiber laser source itself is not Fourier transform-limited [48]. It is because the laser is a package of a CPA system where, again, Yb:fibers are used as a high gain media in both the oscillator and amplifier. Therefore, gain narrowing, high order dispersion or other non-linear effects that may happen in the laser can be one of the possible reasons. Finally, strong non-linear effects, for example self phase modulation, in the PCF for SC generation and fiber amplifiers can limit the compressed pulse-width as well. In practice, the Yb:fiber laser is not stable from moment to moment when the compression was performed. Therefore, it is better for the two colors to be compressed at the same time. This was impossible in reality.

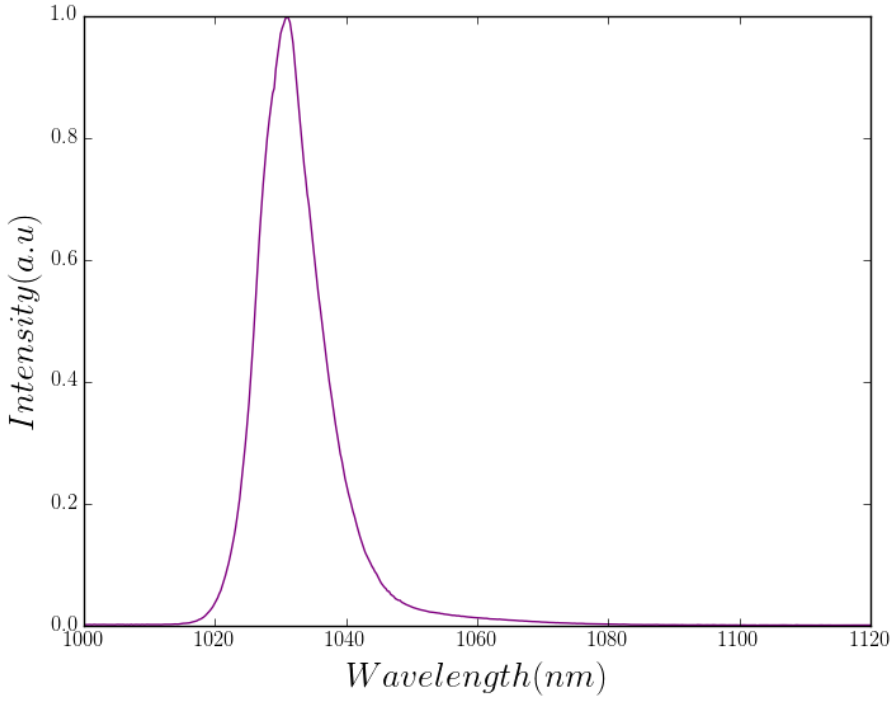

Figure 4.9: ASE spectrum of the main Yb:fiber amplifier in the case of no seeding

In general, mixing different frequencies for down frequency conversion in a nonlinear crystal, like GaSe in our case, can cause constraints in MIR power. First of all, it is noticeable that there is a limitation in the number of nonlinear crystals which have a wide range transparency, i.e., 1-20 μm. It is because, for DFG method, the crystal must be able to transmit all the input (IR) and output (MIR) wavelengths. Besides, the wavelengths on the sides of the range, such as 18.5 μm, has lower transparency than the central wavelengths. Secondly, each crystal itself has different conversion efficiency. For example, GaSe has higher efficiency of conversion than $AgGaS_2$ [53]. Finally, the focused beam area A should be carefully considered to optimize the efficiency but at the same time not to pass the crystal's threshold. This includes intensity threshold for not only two photon absorption (TPA) but also crystal surface damage. K.L Vodopyanov *et al.* found that, for GaSe, the former is 100 MW/cm^2 while the latter should not exceed 1 J/cm^2 or 7 GW/cm^2 for 70 ps pulses [54]. Applying these findings into the case of 1025 and 1085 nm, at 65 MHz, the damage thresholds are 0.54 TW/cm^2(for the 1025 nm) and 0.8 TW/cm^2 (for the 1085 nm). It means that the beam radius focused on GaSe should not be smaller than 1.4 μm due the damage threshold and 104 μm due to TPA limitation for 1025 nm. It is obvious that focusing the beams by 25 cm focal length lens did not pass either the restriction. However, the beam size for optimum efficiency is limited by walk-off angle and, hence, interaction or aperture length. The walk-off angle for the wavelength of 1025 nm is theoretically estimated to be 3.48^0 for type I phase matching and 3.6^0 for type II phase matching according to equation (54). Accordingly, in order that the interaction length calculated by equation (53) is not longer than the crystal length, 1 mm, the beam radius should be less than or equal to 34 μm. Nevertheless, when decreasing the focused beam spot, theoretically, more MIR might be generated, detecting it is another issue. It is because the MIR beam diverges quickly. For example, when the beam was focused by the 25 cm focal length lens, the focused beam diameter was calculated to be around 60 μm for the pump beam and nearly 66 μm for the signal beam. At a distance 10 cm away from the GaSe crystal, or at the spherical mirror, the MIR beam diameter is almost 3 cm which 50% bigger than the mirror diameter. Therefore, not all of the generated MIR was detected at the MCT. Moreover, as we discussed in the experimental setup section for the MIR generation, the thermal detector has to be put further away, approximately 5 cm from the position where the MIR is focused. The beam diameter at the power-meter will be around 1.5cm, while the thermal detector has an active aperture of 1.2 cm in diameter. So, the MIR experiences a loss from the spherical mirror and the power-meter.

4.4 Timing Jitter Measurement: Results and Discussion

For the timing jitter measurement, all the measurements had to be performed as quickly as possible while the laser performance did not change by itself or due to the lab's temperature and humidity fluctuation. The laser performance can change in terms of its pulse-width and/or average output power.

Firstly, an interferometric autocorrelation was performed to achieve the ratio 8:1 between the peak intensity and the background to ensure that alignment was good. Next, the optical cross correlation was carried out for pulse-to-pulse timing jitter measurement. The autocorrelation width of the same pulse and cross correlation width of adjacent pulses are shown in Figure 4.10 and 4.11. The average autocorrelation width and cross correlation width were found to be 400 and 600 fs, respectively. The individual measurements and their corresponding mean values (solid lines) were rescaled and drawn in the same graph to help illustrate the distribution of the measured width with respect to their mean values. Note that any single autocorrelation width did not reveal any fact about the timing jitter happening in the laser source. It is the difference between that of the autocorrelation and cross correlation width that matters. For a better visualization, all the measured widths were put in the same graph with the same scale but, note that in each of the i^{th} measurement, shown in Figure 4.12, the same pulse and adjacent pulse correlation were not measured simultaneously, instead, all the autocorrelation measurements were completed first, then the a series of cross correlation was measured later. As can be seen from Figure 4.12, the cross correlation is broader than the autocorrelation. The broadening was caused by the timing jitter which can be found by using equation (43). It was calculated to be nearly 447 fs. This means that the repetition rate of the Yb:fiber laser was not stable enough for a frequency comb generation.

In terms of measurement precision, as it can be seen from Figure 4.10 and Figure 4.11, the autocorrelation widths fluctuate less from their average value but the adjacent-pulse correlation widths have bigger fluctuation compared to their mean value. Besides, the calculated standard deviation in the former case is nearly 1.2 % while the deviation of the latter is almost 32 % by using the following formula:

$$\sigma = \sqrt{\frac{\sum_{i=1}^{N} |\tau_i - \bar{\tau}|^2}{N}} \tag{62}$$

where τ_i, $\bar{\tau}$ are, respectively, the i$^{\text{th}}$ measured widths and mean width, σ and N are standard deviation and the number of measurements.

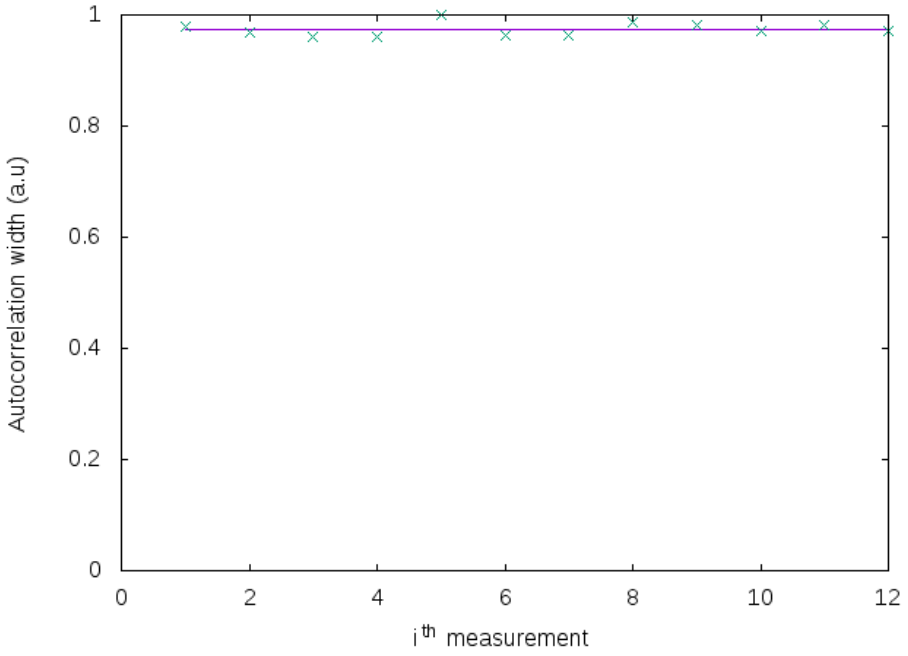

Figure 4.10: Autocorrelation width of the pulse

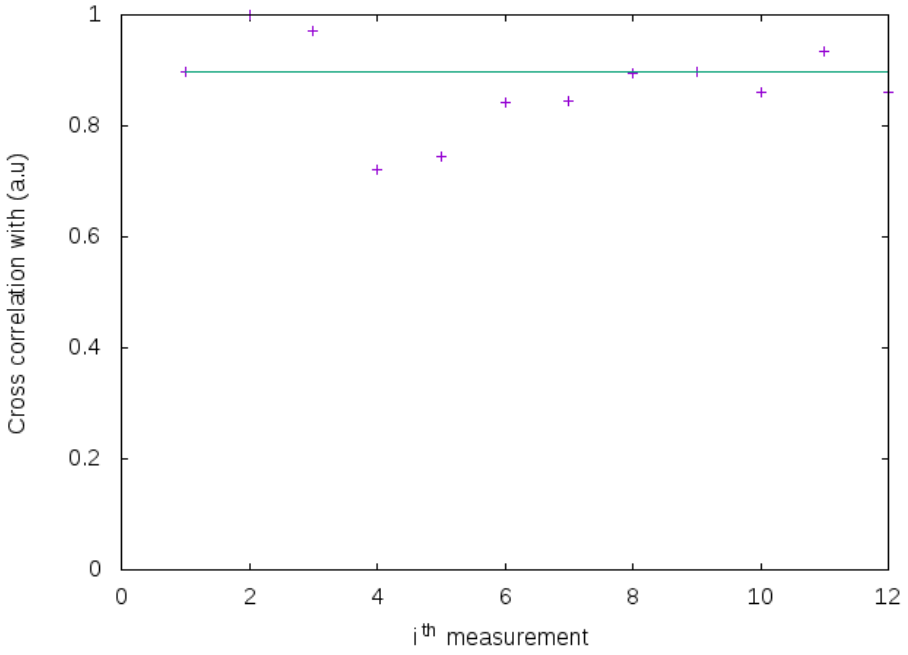

Figure 4.11: Cross correlation width of the adjacent pulses.

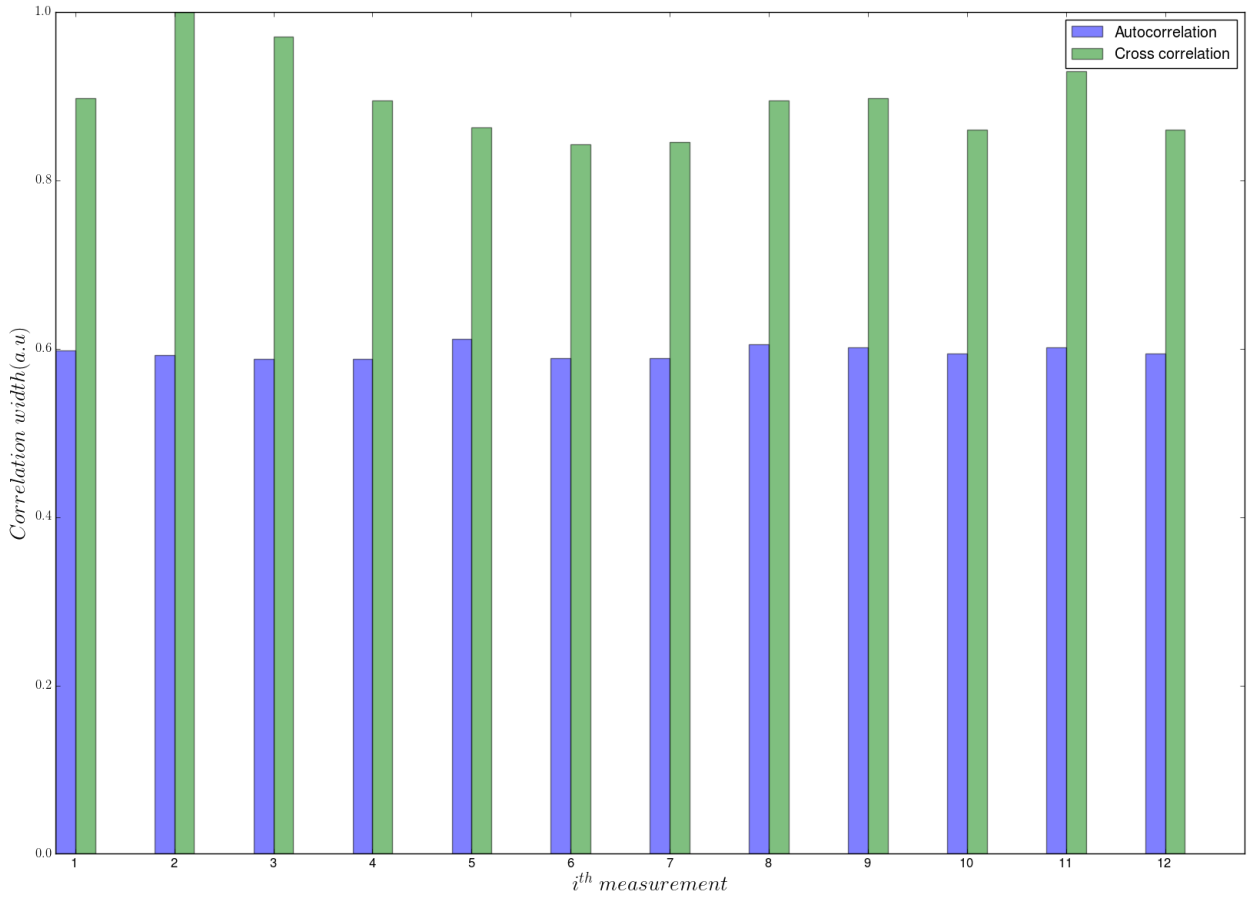

Figure 4.12: Autocorrelation width and cross correlation width

This means that the cross correlation is much less precise than the autocorrelation measurement. At first, this may lead to a thought that it might be too early to conclude that it is impossible for the laser oscillator to make MIR comb because the relative difference between the intensity autocorrelation and cross correlation width is big, 50%. However, from the data shown in Figure 4.12, if we compare the smallest width of an adjacent-pulse correlation width measurement to the average same-pulse correlation width, the smallest relative difference is approximately 41 %. This concludes that, first, it is the fluctuation amongst the measurements made in the case of cross correlation that is big, and, second, the relative difference between the two cases cannot smaller than 40 %.

It is necessary to discuss about the causes of this fluctuation. The first cause is that the sum frequency has significantly low power for the oscilloscope to show the accurate values. The sum frequency's power in the cross correlation is around 3 μW. This low power is a result of the power loss through many reflections by mirrors in the long arm in comparison with the same-pulse measurement. The reason why many mirrors were used in the long

arm is to reduce the space used for the whole setup so that the setup can be put in a box to avoid any small mechanical disturbance caused by the air-flow in the lab. This idea is to help increase the stability and, thus, decrease the measurement errors. The second reason can come from the oscillator itself. In fact, the Yb:fiber in the oscillator is sensitive to any change in temperature, humidity and pumping power. These changes can result in a change in the Yb:fiber's refractive index, and hence, the optical path length in the oscillator. Eventually, there is a variation in the laser period, in other words, a fluctuation in the repetition rate. Moreover, the Yb:fiber laser that is currently being used is not stable in terms of its mode-locking stability and its pulse-width. In order to keep it to be mode-locked, the pump power was changed manually via its current. A rise in the pumping power actually contributes more to the jitter due to its ASE change. Furthermore, from moment to moment, the mode-locking stability is not the same. In addition, the laser's pulse-width can increase by itself from 200 fs to 1 ps. In spite of the fact that the rise does not occur instantaneously, still probably, this might slowly and gradually occur over the time when the experiment was performed. This is definitely out of our control currently.

As the goal of this measurement is to serve for the long-term research goal: making frequency comb at 18.5 μm. In order to have the comb at this wavelength, the cavity length fluctuation should be less than $\frac{\lambda_{MIR}}{2} \approx 9\mu$m. This is equivalent to a jitter of less than 30 fs. In consequence, our Yb:fiber laser cannot work for project of MIR frequency comb generation. Further work of stabilizing the laser should be done, which is beyond of this thesis.

5 Conclusion

In conclusion, in this thesis, a compact CPA system with high average output power as well as a MIR generation at around 18.5 μm based on DFG were developed. In addition, the optical cross correlation was used to measure the timing jitter of the Yb:fiber.

Firstly, the CPA system built in this thesis was very compact and highly stable compared to our previous work [16]. This compact size was accomplished by improving our setup. In particular, a CFBG was used to replace the notch filter in the two-color generation process. In addition, most of the fibers were spliced together and grating stretcher was removed. As a result, this leads to a significant increase in the stability of the whole system. Due to the sharp and clear cut of the CFBG, a 60 nm separation between the two colors, 1025 and 1085 nm, was achieved. In the pre-amplification and main amplification stages, the two diode pumps peaked at 975 nm were thermally controlled in order that the pumping and amplification efficiency could be improved. The pump powers were approximately 6.5 W. As a result, nearly 900 mW of average power was obtained after the pre-amplifier. The input power for the preamplifier was around 25 mW, which was relatively high because of the high power supplied by the Yb:fiber laser. The input of the main amplifier had a range from 150 to 250 mW. Accordingly, the highest average power obtained in the main amplifier was around 3.5 W. The input spectrum of the pre-amplifier and main amplifier, or to be more precise, the spectral ratio between the two colors could be changed due to the HWP in front of the PCF and after the pre-amplifier, respectively. This is a benefit for the main amplifier and MIR generation. After the main amplifier, a ratio short:long of 2:1 was achieved. In terms of the pulse width, the initial pulse width of the seed coming from the laser was estimated to be 200 fs. After the grating compressor, the 1025 nm wavelength had a width of 900 fs while the pulse width of the 1085 nm signal was 600 fs.

Secondly, the MIR was synthesized by mixing the two different frequencies in the nonlinear crystal GaSe. The MIR at 18.5 μm was generated by mixing the pump at 1025 nm and the signal at 1085 nm. The corresponding input power of the signal and the pump was 0.7 and 1.4 W, respectively. The generated MIR, then, was detected by the MCT. It was optimized to 1.4 V. The MIR average power of 150-180 μm was measured by a thermal detector.

Finally, an optical cross correlation was employed to measure the repetition rate fluctuation in the time domain. Theoretically, this timing jitter equals square root of the difference between the squared autocorrelation and squared cross correlation. Therefore, both autocorrelation and cross correlation widths were experimentally measured. The cross

correlation was the correlation between the two adjacent pulses. The average autocorrelation width was around 400 fs while the cross correlation width is 50% longer, nearly 600 fs. This such long cross correlation width is a result of the timing fluctuation from pulse to pulse. The timing jitter is around 450 fs. This means that the current Yb:fiber laser is not qualified or eligible for making a frequency comb yet until some repetition rate stabilization is done.

List of Publications

Peer-reviewed publications

X. Su, **T. Hoang**, P. Long, Y. Zheng, D. Strickland, "A Compact High-Average-Power Femtosecond Fiber-Coupled Two-Color CPA System," *IEEE Journal of Selected Topics in Quantum Electronics,* vol 24, pp. 1-5, September/October 2018.

Conference papers

X. Su, **T. Hoang**, P. Long, Y. Zheng, D. Strickland, "A Compact Watt-Level Sub-Picosecond Fiber-Coupled Dual-Wavelength CPA Laser System," *Photonics North (PN), IEEE*, 2018.

References

[1] S. T. Cundiff, J. Ye, "Colloquium: Femtosecond optical frequency combs," *Reviews of Modern Physics* , vol. 75, pp. 325-342, January 2003.

[2] https://www.rp-photonics.com/frequency_metrology.html, retrieved 10:30AM 18 August 2018

[3] Th. Udem, R. Holzwarth and T. W. Hänsch, "Optical frequency metrology," *Nature*, vol. 416, pp. 233-237, March 2002.

[4] Y. L. Coq, "Optical frequency combs and optical frequency measurements," Dissertation, Université Pierre et Marie Curie-Paris VI, 2014

[5] J. Ye and S. T. Cundiff, *Femtosecond optical frequency comb: principle, operation and applications*. Springer Science & Business Media, 2005.

[6] K. Yamanouchi, K. Midorikawa, *Progress in ultrafast intense laser science*, volume IX, Springer-Verlag Berlin Heidelberg 2013.

[7] A. Schliesser, N. Picqué and T. W. Hänsch, "Mid-infrared frequency combs," *Nature Photonics,* vol 6, pp. 440-449, July 2012.

[8] A. Gambetta, N. Coluccelli, M. Cassinerio *et al.,* "Milliwatt-level frequency combs in the 8–14 μm range via difference frequency generation from an Er: fiber oscillator," *Optics letters* , vol 38, pp. 1155-1157, July 2013.

[9] A. Krier, *Mid-infrared semiconductor optoelectronics.* Springer-Verlag London Limited, 2006.

[10] V. Ulvila, "New method to generate mid-infrared optical frequency combs for molecular spectroscopy," Dissertation, University of Helsinki, Department of Chemistry, Finland, 2018.

[11] A. Ruehl, A. Gambetta *et al.,* "Widely-tunable mid-infrared frequency comb source based on difference frequency generation," *Optics letters,* vol 37, pp. 2232-2234, June 2012.

[12] M. Zimmermann, C. Gohle *et al.,* "Optical clockwork with an offset-free difference-frequency comb: accuracy of sum-and difference-frequency generation," *Optics letters,* vol 29, pp. 310-312, February 2004.

[13] M. Hajialamdari, "Tunable Two-Color Ultrafast Yb: Fiber Chirped Pulse Amplifier: Modeling, Experiment, and Application in Tunable Short-Pulse Mid-Infrared Generation," Ph.D. dissertation, University of Waterloo, Department of Physics and Astronomy, Waterloo, 2013.

[14] R. A. Kaindl, D. C. Smith, M. Joschko, M. P. Hasselbeck, M. Woerner, and T. Elsaesser, "Femtosecond infrared pulses tunable from 9 to 18 µm at an 88- MHz repetition rate," *Optics letters*, vol 23, pp. 861-863, June 1998.

[15] F. Keilmann and S. Amarie, "Mid-Infrared Frequency Comb Spanning an Octave Based on an Er Fiber Laser and Difference-Frequency Generation," *Journal of Infrared Millimeter, and Terahertz Waves*, vol 33, pp. 479-484, 2012.

[16] M. Hajialamdari and D. Strickland, "Tunable mid-infrared source from an ultrafast two-color Yb: fiber chirped-pulse amplifier," *Optics letters,* vol 37, pp. 3570-3572, September 2012.

[17] S. M. Foreman, D. J. Jones and J. Ye, "Flexible and rapidly configurable femtosecond pulse generation in the mid-IR," *Optics letters*, vol 28, pp. 370-372, March 2003.

[18] C. Erny, K. Moutzouris, J. Biegert, D. Kühlke, F. Adler, A. Leitenstorfer and U. Keller, "Mid-infrared difference-frequency generation of ultrashort pulses tunable between 3.2 and 4.8 μm from a compact fiber source," *Optics letters,* vol 32, pp. 1138-1140, May 2007.

[19] T. W. Neely, T. A. Johnson and S. A. Diddams, "High-power broadband laser source tunable from 3.0 μm to 4.4 μm based on a femtosecond Yb:fiber oscillator," *Optics letters*, vol 36, pp. 4020-4022, October 2011.

[20] A. Gambetta, R. Rampgoni, and M. Marangoni, "Mid-infrared optical combs from a compact amplified Er-doped fiber oscillator," *Optics letters,* vol 33, pp. 2671-2673, November 2008.

[21] R. Romero-Alvarez, R. Pettus, Z. Wu and D. Strickland, "Two-color fiber amplifier for short-pulse, mid-infrared generation," *Optics letters*, vol 33, pp. 1065-1067, May 2008.

[22] M. Hajialamdari and Donna Strickland, "Tunable mid-infrared source from an ultrafast two-color Yb: fiber chirped pulse amplifier: erratum," *Optics letters*, vol 43, pp. 353-353, January 2018.

[23] D. Strickland and G. Mourou, "Compression of amplified chirped optical pulses," *Optics communications*, vol 56, pp. 447-449, December 1985.

[24] A. M. Weiner, *Ultrafast optics.* John Wiley & Sons, Inc., Hoboken, New Jersey, 2009.

[25] A. E. Siegman, *Lazers.* University Science Books, Mill Valley, California, 1986.

[26] S. Kane, J. Squier, "Grism-pair stretcher–compressor system for simultaneous second- and third-order dispersion compensation in chirped-pulse amplification," *Optical society of America*, vol 14, pp. 661-665, March 1997.

[27] A. Yariv and P. Yeh, *Optical Electronics in Modern Communications*. Oxford University Press, 2007.

[28] R. Paschotta *et al.*, "Ytterbium-doped fiber amplifiers," *IEEE Journal of Quantum Electronics*, vol 33, pp. 1049-1056, July 1997.

[29] O. Svelto, *Principles of Lasers*. Springer New York Dordrecht Heidelberg London, 2010.

[30] H. M. Pask *et al.*, "Ytterbium-doped silica fiber lasers: versatile sources for the 1-1.2 µm region," *IEEE Journal of Selected Topics in Quantum Electronics*, vol 1, pp. 2-13, April 1995.

[31] E. B. Treacy, "Optical pulse compression with diffraction gratings," *IEEE Journal of Quantum Electronics*, vol 5, pp. 454-458, September 1969.

[32] M. J. F. Digonnet, *Rare-earth-doped fiber lasers and amplifiers*. Marcel Dekker, Inc., 2001.

[33] V. Ter-Mikirtychev, *Fundamentals of fiber lasers and fiber amplifiers*. Springer International Publishing Switzerland, 2014

[34] L. A. Jiang *et al.*, "Noise of mode-locked semiconductor lasers," *IEEE Journal of Selected Topics in Quantum Electron,* vol 7, pp. 159–167, March/April 2001.

[35] J. P. Tourrenc *et al.*, "Experimental investigation of the timing jitter in self-pulsating quantum-dash lasers operating at 1.55 µm," *Optics Express,* vol 16, pp. 17706-17713, October 2008.

[36] L. A. Jiang *et al.*, "Measuring timing jitter with optical cross correlations," *IEEE Journal of Quantum Electronics*, vol 38, pp. 1047-1052, August 2002.

[37] J. P. Tourrenc *et al.,* "Cross-correlation timing jitter measurement of high power passively mode-locked two-section quantum-dot lasers," *IEEE photonics technology letters,* vol 18, pp. 2317-2319, November 2006.

[38] D. R. Dykaar *et al.*, "Mode-locking dynamics of a two-color cross-mode-locked femtosecond Ti:sapphire laser," *International Society for Optics and Photonics*, vol 2116, pp. 98-108, 1994.

[39] R. Trebino, *Frequency-resolved optical gating: the measurement of ultrashort laser pulses*. Springer Science & Business Media, 2012.

[40] I. T. Sorokina, K. L. Vodopyanov, *Solid-state mid-infrared laser sources.* Springer Science & Business Media, 2003.

[41] A. V. Smith, D. J. Armstrong and W. J. Alford, "Increased acceptance bandwidths in optical frequency conversion by use of multiple walk-off-compensating nonlinear crystals," *Optical society of America,* vol 15, pp. 122-141, January 1998.

[42] D. N. Nikogosyan, *Nonlinear optical crystals: a complete survey.* Springer Science & Business Media, 2006.

[43] J. M. Dudley, G. Genty and S. Coen, "Supercontinuum generation in photonic crystal fiber," *Reviews of modern physics,* vol 78, pp. 1135-1184, December 2006.

[44] T. A. Birks, J. C. Knight and P. St. J. Russell, "Endlessly single-mode photonic crystal fiber," *Optics letters*, vol 22, pp. 961–963, July 1997.

[45] L. E. Hooper, P. J. Mosley, A. C. Muir, W. J. Wadsworth and J. C. Knight, "Coherent supercontinuum generation in photonic crystal fiber with all-normal group velocity dispersion," *Optics Express,* vol 19, pp. 4902– 4907, march 2011.

[46] C. DeCusatis and C. J. S. DeCusatis, *Fiber optic essentials.* Elsevier, 2010.

[47] R. Kashyap, *Fiber bragg gratings.* Academic press, 2009.

[48] X. Su *et al.*, "A Compact High-Average-Power Femtosecond Fiber-Coupled Two-Color CPA System," *IEEE Journal of Selected Topics in Quantum Electronics,* vol 24, pp. 1-5, September/October 2018.

[49] D. J. Jones, S. A. Diddams *et al.,* "Carrier-Envelope Phase Control of Femtosecond Mode-Locked Lasers and Direct Optical Frequency Synthesis," *Science,* vol 288, pp. 635-639, April 2000.

[50] https://www.eotech.com/60/application-notes/feedback-prevention-in-optical-fiber-based-ultrafast-lasers-using-eot-isolators, retrieved 10:30AM 29 July 2018

[51] A. M. Al-Kadry and D. Strickland, "Generation of 400 μW at 17.5 μm using a two-color Yb fiber chirped pulse amplifier," *Optics letters,* vol 36, pp. 1080-1082, April 2011.

[52] R. Hegenbarth, "High-power broadband femtosecond near-and mid-infrared sources based on optical parametric oscillators and difference frequency generation at 40 MHz repetition rates," 2014.

[53] S. Ehret, H. Schneider, "Generation of subpicosecond infrared pulses tunable between 5.2 μm and 18 μm at a repetition rate of 76 MHz," *Applied Physics B: Lasers and Optics,* vol 66, pp. 27-30, 1998.

[54] K. L. Vodopyanov *et al.,* "Two-photon absorption in GaSe and $CdGeAs_2$," *Optics Communications*, vol 155, pp. 47-50, 1998.